A metabolic model based on a pangenome core unveils new biochemical features of the phytopathogen *Xylella fastidiosa*

Paola Corbín-Agustí[a] *, Miguel Álvarez-Herrera[a], Miguel Román-Écija[b], Patricia Álvarez[a], Marta Tortajada[c], Blanca B. Landa[b] *, Juli Peretó[a,d]

[a]Institute for Integrative Systems Biology, I2SysBio (CSIC-Universitat de València), Paterna, Spain.

[b]Institute for Sustainable Agriculture (IAS), Spanish National Research Council (CSIC), Córdoba, Spain.

[c]Department of Biomedical Sciences, Faculty of Health Sciences, Universidad Cardenal Herrera, Centro de Estudios Universitarios, UCH-CEU, Alfara del Patriarca, Spain.

[d]Department of Biochemistry and Molecular Biology, University of Valencia, Burjassot, Spain.

*Corresponding authors: Blanca B. Landa blanca.landa@ias.csic.es, Paola Corbín-Agustí paola.corbin@uv.es

Abstract

Xylella fastidiosa is a xylem-limited phytopathogenic bacterium responsible for severe diseases in many economically important crops. Despite its impact, its metabolism remains poorly characterized due to fastidious growth and the limited availability of defined culture media. Here, we reconstruct the first pangenome-based genome-scale metabolic model for *X. fastidiosa*, integrating conserved metabolic functions from 18 strains across five subspecies. The resulting core model, iXfcore, is manually curated and used to explore the species' metabolic capabilities. Model simulations predict minimal nutritional requirements that guided us in the formulation of defined media supporting biofilm formation in vitro, providing validation of the model's predictive capacity. Network analysis also identifies a previously undescribed pathway enabling growth on acetate as a sole carbon source. In addition, the model predicts the overproduction of polyamines, compounds linked to virulence in other phytopathogens. Experimental analyses confirm the production and secretion of polyamines in multiple *X. fastidiosa* strains, providing the first evidence of this capability. These results suggest that polyamine biosynthesis may represent an uncharacterized virulence factor for *X. fastidiosa*, potentially contributing to protection against host-induced oxidative stress. Overall, iXfcore provides a systems-level framework to investigate *X. fastidiosa* metabolism, generate testable hypotheses on its physiology and virulence, and support future strain-specific models and studies of host-pathogen metabolic interactions.

Keywords: *Xylella fastidiosa,* pangenome, metabolic model, polyamines, acetate assimilation, defined medium

1. Introduction

Xylella fastidiosa is a fastidious, Gram-negative, xylem-limited phytopathogenic bacterium that infects more than 700 plant species worldwide (EFSA et al., 2026), including several crops of major agro-economic relevance. In some of these hosts, the bacterium causes devastating diseases such as Pierce's disease in grapevine, citrus variegated chlorosis, almond leaf scorch, and olive quick decline syndrome (EPPO, 2023). The bacterium colonizes the xylem vessels of its plant hosts, and symptoms development depends on several bacterial virulence factors, particularly the formation of biofilm and host defense responses (Landa et al., 2022; De La Fuente et al., 2024). Biofilms also develop in the anterior foregut of sap-feeding insect vectors, which mediate bacterial transmission (Chatterjee et al., 2008).

X. fastidiosa is also characterized by substantial intraspecific diversity. Recent computational analyses support a revised taxonomy that groups the species into three major clades: clade I (corresponding to subsp. *pauca*), clade II (subsp. *multiplex*) and clade III (including three subsp.: *fastidiosa*, *morus* and *sandyi*) (Denancé et al., 2019). In parallel, multilocus sequence typing (MLST) has been widely used for the epidemiological characterization of strains (Scally et al., 2005) with 90 sequence types (STs) have been described to date (Jolley et al., 2018; EPPO 2023). Although STs do not provide genome-wide resolution and therefore cannot capture the full extent of gene-content variation, they remain useful for rapid strain typing, subspecies assignment, and initial epidemiological interpretation. However, the high recombination rates and the existence of some non-monophyletic STs raise concerns about the phylogenetic resolution and the robustness of current classification schemes based solely on MLST (Hanage et al., 2005; Vanhove et al., 2019; Landa et al., 2020). This genomic complexity suggests that marker-based classification alone is insufficient to infer functional traits, including metabolic capabilities that may influence host association, niche adaptation, and pathogenicity (Landa et al., 2022).

Despite decades of research, key aspects of *X. fastidiosa* physiology –particularly those linked to virulence, host adaptation, and nutritional requirements– remain poorly understood. This knowledge gap is especially relevant because the bacterium inhabits the xylem, a nutritionally restricted environment in which successful colonization, multiplication, and biofilm formation are expected to depend strongly on metabolic adaptation. Its inability to grow efficiently on standard bacteriological media, reflected in the species epithet "*fastidiosa*", continues to be a defining feature of the species (Davis et al., 1981; Wells et al., 1987; Chatterjee et al., 2008). Empirical efforts have produced improved culture media that support faster growth (Davis et al., 1980; Wells et al., 1981; Davis et al., 1981; de Macedo Lemos et al., 2003), but none fully

overcome its fastidiousness (Campanharo et al., 2003). Moreover, growth in currently available defined media remains slow and biomass production is limited. As a result, the metabolic basis of nutrient use, physiological specialization, and virulence-associated traits in *X. fastidiosa* is still only partially resolved (De La Fuente et al., 2024).

Genome-scale metabolic models (GEMs) are structured knowledge bases that integrate biochemical, genetic and genomic data into a system-level representation of the metabolic capabilities of an organism (O'Brien et al., 2015). Over the past two decades, GEMs have been applied in systems biology, enabling in silico prediction of genotype-phenotype relationships, reverse ecology paradigm to infer ecological features from genomic data, such as nutrient requirements prediction and growth medium design, and the discovery of metabolic network properties or pan-reactome comparisons (Yus et al., 2009; Monk et al., 2014; Gu et al., 2019; Ye et al., 2022; Qian & Ye, 2024). Constraint-based reconstruction and analysis (COBRA) is one of the foundational and most widely used approaches for working with GEMs. It achieves high predictive power by imposing physicochemical and environmental constraints (such as stoichiometry, thermodynamics and nutrient availability) that define a solution space encompassing all feasible metabolic states of the cell under different conditions (Ibarra et al., 2002; Palsson, 2015).

Here, we present an in silico approach to investigate key aspects of *X. fastidiosa* physiology through the reconstruction of a GEM. Although two metabolic models have previously been reconstructed for this phytopathogen, both are strain-specific (Gerlin et al., 2020; Oliveira et al., 2023). In this study, to account for its remarkable intraspecific genetic diversity while focusing on its conserved metabolic functions, a pangenome was assembled and used it as the template for a core metabolic model reconstruction. The resulting model–iXfcore–represents a species-level GEM that reflects metabolic functions conserved across *X. fastidiosa,* rather than traits restricted to particular subspecies or strains. Then, this reconstruction was experimentally validated by growth-phenotype profiling of a selection of *X. fastidiosa* strains. We also used the iXfcore model to design a defined minimal growth medium based on predicted nutritional requirements–an aspect that has received limited attention despite *X. fastidiosa* being the first phytopathogenic bacterium with a fully sequenced genome (Simpson et al., 2000). Beyond this, the metabolic network highlighted two notable features of the bacterial physiology. First, given the absence in *X. fastidiosa* of previously described acetate assimilation pathways, we sought a metabolic solution that would explain growth on acetate as the sole carbon source. That solution emerges from the combination of other metabolic submodules, providing genomic support for acetate utilization suggested by model-based analyses. Second, the iXfcore model predicts a remarkable capacity for polyamine

biosynthesis. Polyamines are metabolites that are not only produced by plants as part of their oxidative stress and defense responses, but have also been previously linked to virulence in other phytopathogens such as *Ralstonia solanacearum* (Lowe-Power et al., 2018) and *Pseudomonas syringae* (Solmi et al., 2025). In this study, we experimentally confirmed polyamine production in *X. fastidiosa* for the first time, suggesting a possible role in host-pathogen interactions. Together, this work delivers the first species-level GEM of *X. fastidiosa* and establishes a systems biology framework to investigate its physiology, nutritional requirements, and metabolic determinants of pathogenicity.

2. Materials and Methods

2.1. Genome data preparation and pangenome reconstruction

A total of 18 *X. fastidiosa* strains belonging to five subspecies were considered for the pangenome assembly (Table 1). Complete, chromosomal, whole-genome data was retrieved from the NCBI Genome database (Sayers et al., 2024). For each strain, the associated plasmid sequences, when available, were also inspected using the BlastKOALA annotation server (Kanehisa et al., 2016) and the NCBI annotation. As none of the plasmid-encoded genes were associated with relevant metabolic functions, plasmid sequences were excluded from the pangenome analysis. Coding sequences, excluding those annotated as pseudogenes, were clustered into ortholog groups (OGs) using InParanoid (Remm et al., 2001), applying a minimum of 80 % sequence identity and at least 50 % pairwise aligned sequence length, using the BLOSUM 80 substitution matrix. Pairwise OGs generated by InParanoid were merged into multi-strain OGs using QuickParanoid (http://pl.postech.ac.kr/QuickParanoid/). Genes without a best bidirectional hit in any other genome were classified as “unique” while “accessory” genes were defined as those present at least in two strains. Genes belonging to OGs shared across all strains were considered “core”. Core, accessory and unique gene sets were annotated with BlastKOALA automatic annotated server to explore the functional traits.

2.2. Metabolic model reconstruction and refinement

For COBRA, established protocols were followed (Thiele & Palsson, 2010; Nogales, 2017). An initial draft reconstruction of the metabolic network was generated based on the core gene set of the *X. fastidiosa* 9a5c strain using the automatic workflow provided by ModelSEED

(Overbeek et al., 2005; Henry et al., 2010). In addition, draft reconstructions were generated for all remaining strains to support the manual curation of the core draft model. Curated genome-scale metabolic models of *Escherichia coli* iJO1366 (Orth et al., 2011) obtained from BiGG Models (King et al., 2016), *X. fastidiosa* Xfm1158 (Gerlin et al., 2020) and iMS508 (Oliveira et al., 2023) from BioModels (Malik-Sheriff et al., 2020), and *Xanthomonas campestris* pv. *campestris* str. B100 (Schatschneider et al., 2013) were used as references during the curation process. Subsequently, the model was iteratively refined to ensure consistency with available physiological and biochemical data (see Supplementary Methods: Metabolic model refinement).

In parallel with the rest of the network, the biomass reaction was also curated, using as template the one generated by ModelSEED. The suitability of each metabolite in the template and potential biomass components were evaluated, including the molar contribution of each one, based on biochemical data and the biomass reactions from the reference models. Manipulation of metabolic reconstructions was carried out with the COBRApy library in Python (Ebrahim et al., 2013). NetworkX v2.4 (Hagberg et al., 2008), Escher v1.7.3 (King et al., 2015), yED Graph Editor v3.18.2 (yWorks GmbH, 2020) and Cytoscape v3.7.1 (Shannon et al., 2003) were used for metabolic network visualization during the curation process. The quality of the final model was evaluated using the MEMOTE v.0.13.0 tool (Lieven et al., 2020). The final GEM is provided in JSON, MAT-File and Systems Biology Markup Language (SBML) formats (Supplementary Material S1).

2.3. In silico constraints and growth conditions

For reversible reactions, upper and lower bounds of 1000 and -1000 $mmol \cdot gDW^{-1} \cdot h^{-1}$, were respectively applied. For irreversible reactions, the lower (or upper) bound was fixed at 0 $mmol \cdot gDW^{-1} \cdot h^{-1}$. Maximization of growth rate was set as the objective function, leaving oxygen exchange unconstrained. The growth-associated maintenance energy (GAM) was fixed at 50.12 $mmol \cdot gDW^{-1} \cdot h^{-1}$, while the non-growth-associated maintenance energy (NGAM) was set to 3.073 $mmol \cdot gDW^{-1} \cdot h^{-1}$, according to Gerlin et al. (2020).

For simulation of growth conditions, the lower bounds of exchange reactions were set to zero except for the inorganic ions included in the predicted minimal medium. For minimal medium simulations, glutamine uptake flux was constrained to -7.25 $mmol \cdot gDW^{-1} \cdot h^{-1}$ as the carbon and nitrogen source, based on environmental, biochemical and previous metabolic modeling data (Davis, 1992; Gerlin et al., 2020; Orth et al., 2011). For trade-off simulations, glutamine

177 uptake was fixed at -15.665 mmol·gDW^{-1}·h^{-1}. More information can be found in Supplementary
178 Methods: In silico constraints and growth conditions.

179

180 ## 2.4. Flux Balance Analyses

181 Flux Balance Analysis (FBA) and parsimonious Flux Balance Analysis (pFBA) were performed
182 using the COBRApy software (Ebrahim et al., 2013). The optimization problems were solved
183 with the GNU Linear Programming Kit (GLPK) v.5.0 or the IBM ILOG CPLEX Optimizer
184 v.22.1.1. FBA and pFBA were used to compute the maximum value of the objective function
185 and the corresponding flux distribution (Orth et al., 2010; Thiele & Palsson, 2010).

186

187 ## 2.5. Design of synthetic defined minimal media

188 To design a model-driven minimal medium sustaining the FBA-predicted growth rate under
189 the fixed L-glutamine uptake constraint, the number of active exchange reactions was
190 minimized. This was formulated as a mixed-integer linear programming (MILP) problem and
191 solved using the GLPK solver, employing the *minimal_medium* implementation from the
192 COBRApy medium module (Ebrahim et al., 2013). Based on the predicted metabolite
193 requirements, six synthetic defined minimal media were designed (mXC1-mXC6, Table S1).
194 The initial formulations (mXC1 and mXC2) were derived from the in silico minimal medium,
195 using glutamine as carbon and nitrogen source, and different iron sources. For subsequent
196 formulations (mXC3 to mXC6), glutamine was replaced with equivalent quantities of
197 alternative carbon sources (sodium acetate or ribose), supplementing with nitrogen sources.
198 Generally, ammonium sulfate was used as an inorganic nitrogen source, whereas cysteine
199 was used as an alternative nitrogen source in mXC6 formulation. To validate the biotin-related
200 predictions under growth on acetate, mXC4 medium was supplemented with biotin.
201 Concentrations of all components were adapted from existing media known to support *X.*
202 *fastidiosa* growth. Concentrations of glutamine, hemin chloride and inorganic salts were
203 adapted from PW synthetic medium (Davis et al., 1981), while ferric pyrophosphate
204 concentrations were derived from BCYE (Wells et al., 1981) and 3G10R media (Leite et al.,
205 2004). Concentration of $(NH_4)_2SO_4$ was obtained from XVM2 medium (Hiery et al., 2013),
206 cysteine from BCYE and XF-26 (Chang, 1993), and biotin from SXM (Neumann, 2003). All
207 media were adjusted to a pH of 6.9 and brought to a final volume of 1 L with sterile distilled
208 water. PD3 broth (Davis et al., 1981) was selected as the reference medium because it is
209 widely used for routine cultivation of *X. fastidiosa*, and served as a positive growth control.

210

211 ## 2.6. Acetate assimilation pathways research

212 To investigate the metabolic strategy employed by *X. fastidiosa* for the conversion of acetate
213 into biomass, the diverse metabolic assimilation pathways described in the literature were
214 searched against the *X. fastidiosa* genome. Reference protein sequences corresponding to
215 the enzymatic steps involved in each pathway were retrieved from the BRENDA database
216 based on their associated EC numbers. Reciprocal BLASTP (v2.9.0+) (Camacho et al., 2009)
217 searches were conducted between these reference sequences and the annotated amino acid
218 sequences of *X. fastidiosa*. Substantial outcomes were obtained by setting specific filtering
219 parameters (coverage greater than 80 %, e-value $\leq 10^{-6}$). Additionally, hmmscan, hmmsearch
220 and pfamscan (Madeira et al., 2024) were used to identify conserved protein domains and
221 domain architectures, providing additional support for functional inference. Finally, the results
222 were manually revised and some selected candidates and enzymatic activities were reviewed
223 using the UniProt database (UniProt Consortium, 2025) to validate results.
224

225 ## 2.7. Polyamine and virulence factors trade-off prediction

226 Polyamine biosynthesis and degradation pathways were manually curated and revised as
227 described in the Supplementary Methods metabolic model refinement section. Special
228 attention was paid to S-adenosylmethionine (SAM) regeneration and the L-methionine
229 salvage pathway. As no experimentally validated polyamine export mechanism has been
230 described in *X. fastidiosa*, demand reactions for putrescine, spermidine, and spermine were
231 incorporated to simulate intracellular production and secretion potential.

232 To investigate potential trade-offs between biomass production, polyamine secretion and
233 virulence factors synthesis (EPS and LesA protein), a two-step optimization strategy was
234 applied. First, an experimental-like scenario was reproduced constraining biomass production
235 (0.1608 h^{-1}), EPS biosynthesis (1.296 $mmol \cdot gDW^{-1} \cdot h^{-1}$) and LesA production (0.0024
236 $mmol \cdot gDW^{-1} \cdot h^{-1}$) as described in Gerlin et al. (2020). Under these constraints, glutamine
237 uptake was minimized, resulting in a flux of -15.665 $mmol \cdot gDW^{-1} \cdot h^{-1}$. This value was used as
238 the carbon and nitrogen source uptake for all trade-off simulations. In the second step,
239 biomass was constrained to a minimum of 0.1608 h^{-1}, and the feasible production space of
240 the three target metabolites was explored. For each metabolic product, the maximum
241 achievable flux at the minimum fixed biomass level was determined by FBA by maximizing
242 the corresponding demand or export reaction. Uniform grids (30 intervals per axis) ranging

243 from zero to the maximum achievable flux were generated for each metabolite. For every
244 combination of target fluxes, biomass was constrained to a minimum value of 0.1608 h^{-1} and
245 the model was re-optimized maximizing the growth rate as the objective function using the
246 CPLEX Optimizer. Only feasible solutions were retained. This sampling enabled the
247 reconstruction of two-dimensional phase planes approximating the surface of a Pareto front,
248 representing the trade-off between metabolite production and biomass growth rate. Phase
249 planes were obtained by fixing one product to zero and projecting the feasible region of the
250 remaining two metabolites. The resulting solution space was visualized using tricontour and
251 tricontourf functions from the Matplotlib library. Biomass flux was represented as a continuous
252 color gradient.

253

254 **2.8. Bacterial strains and culture conditions**

255 Seven *X. fastidiosa* strains were used in the different in vitro studies: two from subspecies
256 *fastidiosa* isolated from grapevine in California (Temecula1) and Mallorca, Spain (IVIA5770);
257 three from subspecies *multiplex* isolated from almond trees in Alacant, Spain (ESVL and
258 IVIA5901) and wild olive in Mallorca (XYL468); and two from subspecies *pauca* isolated from
259 olive trees (De Donno and XYL1961/18) in Puglia, Italy, and Eivissa, Spain, respectively.
260 Stocks of *X. fastidiosa* strains were stored in phosphate buffered saline (PBS) plus 50 %
261 glycerol at -80 °C. For all the experiments, strains were recovered from glycerol stocks on
262 plates of PD3 (Davis et al., 1981) or BCYE (Wells et al., 1981) media incubated at 28 °C in
263 the dark. After 6 to 8 days, cells were re-streaked onto new plates and cultured for 5 to 7 days
264 before using them in each experiment.

265

266 **2.9. Growth of *Xylella fastidiosa* strains in synthetic defined media**

267 The potential utilization of 190 carbon sources of five *X. fastidiosa* strains (ESVL, De Donno,
268 IVIA5901, Temecula1, and XYL1961/18) was determined using the PM1 and PM2 Biolog
269 phenotype microarray (PM) system (Biolog, Hayward, California) (Supplementary Methods-
270 Phenotypic characterization of *Xylella fastidiosa* strains).

271 In vitro culture experiments using the six minimal media described in section 2.5 (Table S1)
272 were conducted with the seven *X. fastidiosa* strains mentioned in section 2.8 as previously
273 described by Román-Écija and coworkers (2023), to assess the ability of the designed minimal
274 media to support bacterial growth, as well as biofilm formation. Briefly, a cell suspension of
275 each strain was diluted in each medium to reach at OD_{600} = 0.08. Cell suspensions (200 µL)

276 were inoculated in polystyrene 96-well microplates (Sarstedt, Nümbrecht, Germany) and
277 incubated at 28 °C during 7 days without agitation. Total bacterial growth was measured daily
278 by measuring OD_{600}. After the 7-days incubation, planktonic phase was discarded and biofilm
279 formation was estimated using the crystal violet assay. At least four independent experiments
280 were conducted, and each experiment included five replicated wells per treatment. Non-
281 inoculated medium served as negative control.

282

283 **2.10. Polyamines production by *Xylella fastidiosa* strains in liquid medium**

284 To validate the metabolic model predictions for the ability of *X. fastidiosa* to produce
285 polyamines during in vitro culture, two experiments were performed. An initial experiment was
286 carried out to determine whether *X. fastidiosa* produces polyamines. For that, 10 mL of cell
287 suspensions at OD_{600} = 0.05 of six *X. fastidiosa* strains (those mentioned in section 2.8, except
288 for IVIA5901) were used to inoculate 50-mL glass flasks and incubated under agitation at 28
289 °C. After 9 days of growth, two types of samples were collected for polyamine extraction. The
290 first one included *X. fastidiosa* cells from planktonic growth plus those present in the biofilm
291 formed on the glass surface at the air-liquid interface. For that, cells were scratched from the
292 attachment ring formed on the glass wall and vortexed. Then, the bacterial cell pellet (CP) was
293 obtained after centrifugation at 14,000 rpm for 10 min of the entire culture. The second type
294 of sample included the culture supernatant (SP). At least two biological replicates for each
295 strain were performed. For the second experiment one strain per subspecies was selected,
296 namely, ESVL, De Donno, and Temecula1. In this experiment, three types of samples were
297 obtained after 5 and 12 days of growth. For each strain and sampling point, culture cells in
298 planktonic growth were collected by transferring the entire culture to a new falcon tube. Then,
299 a cell pellet from planktonic growth (CP-P) and a SP were obtained after centrifugation as
300 described above. To collect cells growing in biofilms, the biofilm formed on the glass surface
301 was scraped with a loop and resuspended with a pipette using 1 mL of sterile distilled water.
302 Then, a cell pellet from biofilms (CP-B) was collected by centrifugation and removal of the
303 supernatant. In this second experiment, four biological replicates for each strain and condition
304 were obtained.

305 The polyamine extraction and quantification of CP-P, CP-B, and SP samples were carried out
306 according to Solé-Gil and coworkers (2019) with small modifications. Briefly, bacterial cell
307 pellets were resuspended in 1 mL sterile water, treated with lysozyme (10 $mg \cdot mL^{-1}$), and kept
308 on ice for 10 min. Subsequently, bacterial cells were disrupted by sonication (10 cycles of 30
309 s each). After centrifugation at 10,000 rpm for 10 min, 500 µL of the supernatants were treated

310 with 2.5 mL of perchloric acid 5 % (w/v). Culture supernatants (2.5 mL) were also treated with
311 2.5 mL of perchloric acid. At this point, pre-treated samples were stored at -20 °C and sent for
312 polyamine analysis to the Metabolomics Service of the Institute of Molecular and Cellular
313 Biology of Plants (IBMCP, Valencia). Before analysis, 500 µL of the internal standard (1,6-
314 hexanediamine 1 mM) were added to each sample. Polyamines were quantified by HPLC
315 analysis as described by Santos and coworkers (2021) in triplicate.

316

317 **2.11. Data processing and statistical analysis**

318 To evaluate growth in minimal media, growth curves were obtained by accumulating OD_{600}
319 values over time from the date of inoculation. The OD_{600} value of the control wells was
320 subtracted from each time point to obtain the net absorbance. Cumulative growth was then
321 calculated by subtracting the initial net absorbance at the beginning of the experiment from
322 the net absorbance on each subsequent day. The standardized area under the growth
323 progress curve (sAUGPC) was calculated using the trapezoidal integration method
324 standardized by duration of the experiment in days (Simko & Piepho, 2012).

325 For SP samples, net polyamine content was calculated by subtracting the mean concentration
326 for each polyamine measured of the non-inoculated negative control medium (PD3). This
327 correction was not applied to the pellet samples, as centrifugation removes the influence of
328 the initial medium. Any negative values after normalization were set to zero.

329 Statistical analyses and data visualization were conducted using R software. Given the
330 variability of bacterial growth and polyamines production, Wilcoxon rank-sum tests were used
331 for all pairwise comparisons ($P \leq 0.05$). For minimal media and biofilm experiments, each
332 tested medium was compared against the PD3 control, and between media pairs sharing the
333 same carbon source. For polyamine data, differences between time points within each sample
334 type and strain were assessed.

335 Data were visualized using violin plots for growth and biofilm formation in minimal media, and
336 polyamine data. For polyamine results, a pseudo-logarithmic scale was used to facilitate
337 comparison across several orders of magnitude. All visualizations were produced using
338 ggplot2, ggpubr and ggh4x packages in R.

339

340 ## 3. Results

341 ### 3.1. Metabolic characteristics of the *Xylella fastidiosa* pangenome and the core
342 metabolic model

343 A curated genome-scale metabolic reconstruction was generated based on the core genes of
344 18 *X. fastidiosa* strains encompassing five subspecies (Table 1), including the strains
345 previously used for metabolic modelling (Gerlin et al., 2020; Oliveira et al., 2023). Host
346 diversity of the selected strains reflects the broad ecological range of the species and provides
347 a representative basis for assessing the pangenomic and metabolic variability of this
348 phytopathogen. Moreover, this pangenome also incorporates recently emerged European
349 strains, with six isolates from Spain, Italy and France, in order to account for the lineages
350 involved in the outbreaks starting to be detected in 2013, which have resulted in substantial
351 agricultural and economic losses in Europe (Sanchez et al., 2019; De la Fuente, 2024).

352 Pangenome analysis revealed a total of 2660 ortholog groups (OGs), comprising 40828
353 genes, of which 1372 OGs included genes found in the 18 strains (Fig. 1A). The core genome
354 consists of 26831 genes, constituting 65.72% of the genes analyzed. The accessory genome
355 includes 13421 genes, corresponding to 32.87% of the total pangenome. Among the analyzed
356 strains, XYL468 exhibited the highest number of accessory genes (890), whereas Salento-1
357 displayed the lowest (595). A total of 576 genes were classified as unique, accounting for
358 1.41% of all genes. The strain with the largest number of unique genes was XYL1961/18, with
359 141 unique genes, while U24D contained only 2 unique genes. Only a limited number of OGs
360 showed strict subspecies-specific distribution.

361 Functional annotation of the pangenome revealed clear differences between the core,
362 accessory, and unique gene sets (Fig. S1). Core OGs were predominantly enriched in
363 metabolic functions, particularly carbohydrate, amino acid, nucleotide, energy and glycan
364 metabolism, as well as metabolism of cofactors and vitamins. These were followed in
365 prevalence by genes associated with genetic information processing and with signalling and
366 cellular processes. In contrast, accessory genes showed a stronger representation of the latter
367 two categories, including a higher proportion of functions associated with prokaryotic defense,
368 secretion and transport systems, and quorum-sensing pathways, alongside a substantial
369 fraction of genes with unknown function. Metabolic genes were also present within the
370 accessory set, although to a lesser extent. For the unique gene set, only 6.2% (36 out of 576)
371 of the genes could be functionally annotated, and none were linked to core metabolic
372 pathways. Instead, the annotated genes mapped to categories such as prokaryotic defense
373 systems, quorum sensing, or DNA replication and repair.

374 The core ortholog set identified in the pangenome was used to generate a draft genome-scale
375 metabolic reconstruction using the automated reconstruction software ModelSEED (Henry et
376 al., 2010). Curation was performed iteratively (see Supplementary Results and Discussion).
377 The features of the final genome-scale metabolic reconstruction (iXfcore; Supplementary
378 Material S1) are summarized in Fig. 1B. From a total of 1034 reactions, 83% are associated
379 with gene-protein-reaction (GPR) rules. Of the reactions lacking GPR associations, 57%
380 correspond to boundary or transport reactions, the majority of which do not require gene
381 assignment. Model quality and consistency evaluated using the Memote testing suite (Lieven
382 et al., 2020), yielded a total score of 85% and a consistency score of 97% (Supplementary
383 Material S2). Annotation completeness scores were 66% for metabolites, 73% for reactions,
384 and 53% for genes. The coverage of SBO terms reached 83%, indicating strong semantic and
385 structural annotation.

386 The core gene set of *X. fastidiosa* encoded almost all central metabolic functions, although
387 several specific gaps and distinctive features were identified (see Supplementary Results and
388 Discussion). Of particular relevance is the absence in all analyzed strains of a glyoxylate cycle,
389 as well as the lack of anaplerotic reactions connecting the intermediates of glycolysis and the
390 TCA cycle.

391 Finally, the biomass reaction was formulated to include all known cellular components and
392 their respective contributions per gram of biomass. Following extensive curation, including
393 comparative evaluation against the biomass formulations of the *E. coli* model iJO1366 (Orth
394 et al., 2011) and the *X. fastidiosa* model Xfm1158 (Gerlin et al., 2020), the biomass equation
395 included 78 metabolites.

396 FBA predicted a maximum specific growth rate of 0.413 h^{-1} when glutamine, one of the major
397 components of xylem sap, was supplied as the sole carbon source at an uptake rate of 7.25
398 $mmol \cdot gDW^{-1} \cdot h^{-1}$ (Supplementary Material S3). The corresponding optimal flux distribution is
399 shown in Fig. 1C. Under these conditions, most of the imported glutamine is converted into α-
400 ketoglutarate. Carbon flux proceeds through the TCA cycle and malate is partially converted
401 to pyruvate via the malic enzyme, generating NADPH. Pyruvate bifurcates toward
402 gluconeogenesis or to the synthesis of acetyl-CoA. The iXfcore model further predicted uptake
403 of inorganic ions, phosphate, and sulfate under these growth conditions, while CO_2 and NH_3
404 were secreted as metabolic by-products. Oxygen was also required, as the model did not
405 predict growth under anaerobic conditions.

406 ### 3.2. Growing *Xylella fastidiosa* in minimal media predicted by the model

407 Empirical efforts have led to the development of several culture media for *X. fastidiosa*,
408 including PD2 (Davis et al., 1980), BCYE (Wells et al., 1981) and PW (Davis et al., 1981).
409 However, these formulations do not fully overcome the fastidious growth requirements of the
410 bacterium. In this work, a reverse ecology approach based on constraint-based metabolic
411 modeling was applied to predict a synthetic defined minimal medium capable of sustaining
412 biomass production in the iXfcore model. Under a fixed L-glutamine uptake constraint (7.25
413 $mmol \cdot gDW^{-1} \cdot h^{-1}$), the minimal medium prediction identified oxygen, phosphate, sulfate,
414 glutamine (as both carbon and nitrogen source), and inorganic ions as required components
415 (see Supplementary Material S4 for the complete list of metabolites and corresponding uptake
416 fluxes).

417 Based on these predicted requirements, six synthetic defined minimal media were formulated
418 (mXC1–mXC6; Table S1). Glutamine was used as the sole carbon and nitrogen source in
419 mXC1 and mXC2, given its abundance in xylem sap. Two different iron sources were tested
420 in these media, ferric pyrophosphate and hemin chloride, to assess iron bioavailability. Acetate
421 was used as the carbon source in mXC3 and mXC4, supplemented with ammonium sulfate
422 as a nitrogen source. To validate model predictions regarding biotin dependency under
423 acetate growth conditions (see section 3.3), mXC4 was additionally supplemented with biotin.
424 Finally, ribose was tested as the sole carbon source in mXC5 and mXC6. In mXC6, cysteine
425 was evaluated as an alternative nitrogen source, as it showed strong utilization in nitrogen
426 assimilation assays (data not shown).

427 All minimal media supported, to some extent, the growth and biofilm formation in all *X.*
428 *fastidiosa* strains studied (Fig. 2; Supplementary Material S4). Interestingly, all strains were
429 able to grow with glutamine media, despite glutamine not supporting growth in the phenotypic
430 characterization of Biolog PM plates (see Supplementary Results and Discussion). The
431 reference medium PD3 significantly supported higher growth than all minimal media across
432 strains (Fig. 2A), except for XYL1961/18, which showed higher growth in the Glutamine+Fe
433 formulation (mXC1) and no significant differences were detected for the rest of the media. In
434 strain XYL468, no significant differences were observed between PD3 and Glutamine+Hemin
435 or Ribose+Cysteine media.

436 Biofilm formation (Fig. 2B) showed comparable levels across most minimal media relative to
437 PD3. The exception was strain De Donno, which produced significantly higher biofilm in the
438 control medium PD3. Overall, a general trend was observed in which synthetic defined media

439 containing ribose supported higher biofilm production across most strains, followed by
440 acetate-based media (Fig. 2B).

441 Pairwise comparisons between media formulations sharing the same carbon source revealed
442 no significant differences for growth or biofilm formation associated with iron source, biotin
443 supplementation in acetate media, or nitrogen source substitution in ribose-based
444 formulations (data not shown).

445

446 ### 3.3. Acetate metabolism in *Xylella fastidiosa*

447 Experimental evidence supports the ability of *X. fastidiosa* to grow on acetate as the sole
448 carbon source in several strains (Gerlin et al., 2020; this work, see Supplementary Results
449 and Discussion). Here, all previously described metabolic solutions to produce biomass from
450 acetate were evaluated, namely: (i) the glyoxylate cycle (Kornberg & Krebs, 1957); (ii) a
451 ferredoxin-dependent pyruvate synthase (Segura et al., 2008), typically associated with
452 anaerobic metabolism; (iii) the ethylmalonyl-CoA (EMC) pathway (Erb et al., 2007); (iv) the
453 methylaspartate cycle (MaC) characteristic of haloarchaea (Khomyakova et al., 2011); and (v)
454 part of the 3-hydroxypropionate (3HP) autotrophic bi-cycle (Herter et al., 2002). Across the
455 18 strains comprising the pangenome, none of these previously described pathways were fully
456 supported by genomic evidence, lacking all or some of the necessary enzymes.

457 The iXfcore metabolic model predicted growth on acetate through an alternative, yet
458 undescribed metabolic solution (Fig. 3). This consisted of a modular pathway with 11 steps
459 (Table S3), connecting acetate to central carbon metabolism, generating pyruvate and
460 succinate and enabling net carbon assimilation into biomass. This pathway integrates two
461 enzymatic subsets present in previously described metabolic routes. The first one
462 corresponds to the initial half of the 3HP bi-cycle, linking acetyl CoA to the synthesis of
463 propionyl-CoA (the remaining reactions of the cycle are absent from the pangenome). The
464 second subset corresponds to the methylcitrate pathway, which enables the assimilation of
465 propionyl-CoA into pyruvate and succinate (Brämer & Steinbüchel, 2001; Dolan et al., 2018).
466 During the reconstruction process, minor gaps were identified in the draft network. These gaps
467 were resolved through manual genome evaluation and literature reviewing. All reactions
468 included in the final pathway are supported by genes present in the pangenome. The putative
469 acetate assimilation pathway in *X. fastidiosa* is represented in Fig. 3 and the Supplementary
470 Results and Discussion file contains a detailed explanation of it.

471 Compared with the flux distribution obtained when glutamine was used as the sole carbon
472 source (Fig. 1C), in the flux distribution corresponding to acetate assimilation (Fig. 3;
473 Supplementary Material S5) pyruvate is no longer converted into acetyl-CoA, as this
474 metabolite is directly generated from acetate (Fig. 3, step 1). The pyruvate generated in the
475 proposed pathway is redirected toward gluconeogenesis, similar to the glutamine-based
476 simulation. Under acetate conditions, the malic enzyme also contributes to NADPH
477 generation, although at 42% of the flux of the one observed with glutamine. This reduction
478 may seem a paradox since the acetate assimilation pathway proposed here shows an
479 increased demand of reducing power. A higher proportion of flux is directed through
480 oxaloacetate (95% vs 27.5% with glutamine). This increased TCA cycle flux implies a higher
481 flux through isocitrate dehydrogenase (IDH). The iXfcore model contains both the NAD- and
482 NADP-dependent IDH isozymes, and when the model was evaluated with pFBA under the
483 same conditions, with acetate 76% of the flux through IDH was generating NADPH, whereas
484 with glutamine as the only C source, all the flux went through the NAD-dependent IDH
485 isoenzyme.

486

487 ### 3.4. Polyamine production by *Xylella fastidiosa* strains

488 The iXfcore model includes the biosynthetic pathways for the polyamines putrescine,
489 spermidine and spermine, including the S-adenosylmethionine (SAM) regeneration cycle
490 required for spermidine and spermine synthesis (Fig. S2). In *R. solanacearum*, putrescine
491 secretion has been experimentally reported (Lowe-Power et al., 2018), although no homologs
492 of known polyamine exporters have been identified in its genome (Igarashi & Kashiwagi, 2010;
493 Sugiyama et al., 2017), suggesting the existence of a yet uncharacterized transport system.
494 Since *X. fastidiosa* lacks any genomic evidence supporting a polyamine export system,
495 cytosolic demand reactions were introduced in the iXfcore model to simulate polyamine
496 overproduction.

497 When polyamine demand reactions were enforced or used as the objective function (see
498 section 2.10), the model predicted feasible production of putrescine, spermidine, and
499 spermine, beyond biomass requirements (Fig. 4A). However, increasing polyamine production
500 resulted in a progressive reduction in biomass flux, revealing a trade-off between growth and
501 polyamine production. The extent of this trade-off varied among the three polyamines, with
502 differences in maximum achievable fluxes at minimum biomass levels. When putrescine
503 overproduction was constrained to zero, spermidine and spermine exhibited a linear inverse
504 relationship, with limited flexibility concerning the production of biomass and combined

505 polyamine (Fig. 4A). In contrast, when putrescine overproduction was allowed together with
506 either spermidine or spermine, a broader feasible solution space for similar biomass levels
507 was observed. In these cases, similar biomass levels could be obtained with different
508 combinations of polyamine production.

509 The experimental results on polyamine production by *X. fastidiosa* strains corroborated the
510 findings of the iXfcore metabolic model (Fig. 4B and Fig. S3; Supplementary Material S6. In a
511 first experiment six *X. fastidiosa* strains belonging to the three subspecies studied in this work
512 produced and secreted polyamines in vitro (Fig. S3). Putrescine, spermidine and spermine
513 were detected in both biofilm and planktonic growth, as well as in the culture supernatant.
514 Spermidine was produced at higher levels than putrescine and spermine. In a second
515 experiment, polyamine levels were analyzed in three distinct sample types: planktonic cell
516 pellets, biofilm-forming cell pellets, and the culture supernatant. Again, spermidine was the
517 most abundant polyamine detected (Fig. 4B). There were no significant differences observed
518 between time points within each sample type, except for the four comparisons marked with an
519 asterisk in Fig. 4B.

520

521 ### 3.5. Trade-off between virulence factors and biomass

522 Previous reconstructions of *X. fastidiosa* metabolism (Gerlin et al., 2020; Oliveira et al., 2023)
523 have considered the secretion of two known virulence factors: the LesA protein (Nascimento
524 et al., 2016) and exopolysaccharides (EPS) (da Silva et al., 2001). The metabolic model of the
525 phytopathogen *R. solanacearum* (Peyraud et al., 2016), also incorporated polyamine
526 secretion. In this work, several scenarios were analyzed by simulating the combined
527 production of LesA, EPS, and one of the detected polyamines: putrescine (Fig. 5A),
528 spermidine (Fig. 5B), or spermine (Fig. 5C). Under these conditions, the model predicted
529 maximum fluxes of 0.02 $mmol \cdot gDW^{-1} \cdot h^{-1}$ for LesA protein, 1.45 $mmol \cdot gDW^{-1} \cdot h^{-1}$ for EPS,
530 7.09 $mmol \cdot gDW^{-1} \cdot h^{-1}$ for putrescine, 1.57 $mmol \cdot gDW^{-1} \cdot h^{-1}$ for spermidine, and 0.87
531 $mmol \cdot gDW^{-1} \cdot h^{-1}$ for spermine.

532 A clear trade-off between virulence factor secretion and biomass production was observed
533 (Fig. 5). The combined production of LesA with EPS showed a linear inverse relationship. For
534 the production of putrescine together with the other virulence factors (Fig. 5A), a nearly linear
535 inverse relationship was observed between the combined production of these compounds and
536 biomass formation. Interestingly, in the case of spermidine (Fig. 5B) and spermine (Fig. 5C),
537 the feasible solution space showed greater compatibility between LesA production and

538 polyamine secretion. In these scenarios, different rates of LesA production remain feasible
539 even when spermidine or spermine are produced at high levels, indicating greater metabolic
540 flexibility for LesA secretion while maintaining the same biomass flux. This behavior is
541 reflected by the broader feasible region observed in the phase planes. In particular, a change
542 in slope appears when LesA production reaches approximately 0.02 $mmol \cdot gDW^{-1} \cdot h^{-1}$. A
543 similar but less pronounced pattern is observed for EPS production. Overall, EPS secretion
544 appears to be more compatible with spermidine or spermine production than with putrescine
545 production, particularly near the upper limit of EPS flux (around 1.3 $mmol \cdot gDW^{-1} \cdot h^{-1}$).

546

547 **4. Discussion**

548 In this work, we reconstructed the core metabolic model of *X. fastidiosa* based on the
549 pangenome of 18 strains belonging to five subspecies of this phytopathogen. This approach
550 accounts for the high genetic diversity within the species while allowing the identification of its
551 conserved metabolic capabilities. Previous metabolic reconstructions of *X. fastidiosa* were
552 strain-specific, including the model for the subsp. *multiplex* CFBP 8418 (Gerlin et al., 2020)
553 and the model for the subsp. *pauca* De Donno (Oliveira et al., 2023). In the first study, genome
554 comparisons were performed with the strains *X. fastidiosa* subsp. *pauca* 9a5c and subsp.
555 *fastidiosa* Temecula1, suggesting that the results could be extrapolated to these subspecies.
556 In contrast, our reconstruction explicitly incorporates these strains within a broader
557 pangenome framework, providing a more robust representation of the conserved metabolic
558 potential of *X. fastidiosa*.

559 Moreover, the iXfcore metabolic model and the pangenome assembly can serve as a
560 foundation for the reconstruction of strain-specific models, following the protocol described in
561 Norsigian et al. (2020). The availability of a curated-base model can significantly reduce the
562 effort required for the generation of multi-strain metabolic models. Such approaches have
563 already been successfully applied to reconstruct models for the *Lactobacillaceae* family and
564 for *Aspergillus fumigatus* strains (Mirhakkak et al., 2023; Ardalani et al., 2024). Additionally,
565 our reconstructed model incorporates the OG associated with each gene in the network
566 annotation, enabling the extraction of strain-specific genetic information when required.

567 *X. fastidiosa* appears to lack typical anaplerotic reactions to replenish the TCA cycle,
568 suggesting that network operation is dependent of an external supply of precursors of the
569 cycle intermediates–such as the amino acids glutamine or glutamate available in the xylem.
570 iXfcore model simulations using hexoses, pentoses or even acetate, are consistent with this

571 observation: without such intermediates, the model cannot sustain growth. In previous
572 reconstructions, different assumptions evaded this issue. Thus, the model by Gerlin et al.
573 (2020) supported growth with the inclusion of the glyoxylate cycle despite without genetic
574 evidence, whereas the reconstruction by Oliveira et al. (2023) allowed a reversible malic
575 enzyme generating malate from pyruvate. If we constrain the malic enzyme to the oxidative
576 decarboxylation direction, restauration of growth requires the presence of a TCA intermediate.
577 In this case, the malic enzyme may contribute to NADPH production in the context of a network
578 with a limited set of reactions for reducing power production. For instance, the in silico
579 simulations indicated that the Entner–Doudoroff (ED) pathway represents the main route for
580 sugar metabolism. This result is consistent with the results of Oliveira et al. (2023) that
581 suggested that this could help protect the bacterium against reactive oxygen species (ROS)
582 generated by the plant defense system (Wang et al., 2017). The generation of NADPH by the
583 ED pathway has been associated with an increased tolerance to oxidative stress in *P. putida*
584 (Chavarría et al., 2013).

585 In axenic cultures, *X. fastidiosa* can grow with acetate as a sole carbon source. Remarkably,
586 acetate is a major organic acid present in olive xylem sap (Anguita-Maeso et al., 2021).
587 Intriguingly, GEMs for this organism lack any canonical pathway for acetate assimilation, and
588 previous metabolic reconstructions have addressed this issue using different strategies. As
589 mentioned before, growth on acetate was enabled in the Xfm1158 model (Gerlin et al., 2020)
590 due to the inclusion of a glyoxylate cycle without genomic evidence of its key enzymes. In
591 contrast, Oliveira et al. (2023) adopted a more conservative position and the iMS50 model
592 cannot simulate growth on acetate. In our reconstruction, the iXfcore model suggested a
593 previously undescribed metabolic solution for acetate assimilation. In brief, we propose the
594 first part of the 3HP bi-cycle–an autotrophic pathway described in *Chloroflexus auranticus* by
595 Herter et al. (2002) (Fig. S4, panel A)–combined with the conversion of propionyl-CoA into a
596 biomass precursor. The assimilation of propionyl-CoA in *X. fastidiosa* would use a pathway
597 different to the one proposed by Zarzycki and Fuchs (2011) for the co-assimilation of acetate
598 in *C. auranticus* (Fig. S4, panel B). Thus, in the iXfcore model propionyl-CoA can be
599 assimilated into pyruvate through the methylcitrate pathway firstly described in yeasts by
600 Tabuchi et al. (1974) and which is also operative in bacteria like *E. coli* grown in propionate
601 (Brock et al., 2002) (Fig. S4, panel C).

602 We can compare this new pathway for acetate assimilation with the ones previously described
603 in the literature (Table S4). The putative acetate assimilation pathway in *X. fastidiosa* (Xf
604 pathway) represents a slight variation of the 3HP pathway described in *C. auranticus*, in terms
605 of energy balance and carbon efficiency; in both cases, there is a net gain of carbon. The main

606 difference is that the Xf pathway involves two more enzymatic steps than the half 3HP bi-
607 cycle. Both pathways are more demanding of reducing power than the rest of known routes
608 and, as discussed before, this may explain the increased flux through the TCA cycle in iXfcore
609 under acetate conditions. It is remarkable that *X. fastidiosa* harbors two structurally different
610 IDH isoenzymes, specific for NAD^+ or $NADP^+$, respectively (Lv et al., 2018). Interestingly, the
611 evolutionary origin of a NADP-dependent IDH has been correlated with an increased demand
612 of reducing power associated with the use of acetate as carbon source (Zhu et al., 2005).

613 Our proposed Xf pathway highlights the role of functional modularity in metabolic adaptation
614 and evolution. Metabolic modules can reorganize or combine to explore biochemical diversity
615 (Schada von Borzyskowski et al., 2020). Functional degeneracy between diverse metabolic
616 solutions also can reflect different dynamics of adaptation to environmental challenges, as
617 described for *Paracoccus denitrificans* (Kremer et al., 2019). On the other hand, in our
618 hypothetical solution for acetate assimilation in *X. fastidiosa* we have proposed several steps
619 catalyzed by enzymes with relaxed substrate specificity. Thus, an acyl-CoA synthetase
620 operates in steps 1 and 5, a citrate synthase is also operative as methylcitrate synthase (step
621 8), and finally aconitase AcnD will act in step 10 (Fig. 3; Table S3; Supplementary Results and
622 Discussion). Those cases would be examples of the well-known metabolic economy observed
623 in symbionts (either pathogens or mutualists), sustained through reactions operated by
624 promiscuous or multifunctional enzymes (Yus et al., 2009; Kim et al., 2010; Gil & Peretó,
625 2015). Gerlin et al. (2020) have correlated the lack of enzymatic redundancy in the *X.*
626 *fastidiosa* metabolic network with a reduced robustness and its characteristic fastidious
627 growth. In any case, we are aware that our in silico hypothesis requires experimental
628 validation, through omics approaches, biochemical characterization of enzyme activities, and
629 ^{13}C-fluxomics experiments. Furthermore, phylogenetic analysis of the involved enzymes also
630 could shed light on the origin and evolutionary tinkering of the pathway, as well as its
631 distribution in the tree of life.

632 Metabolic reconstructions have been previously used to design minimal growth media for
633 fastidious microorganisms. A notable example is the work for *Mycoplasma pneumoniae* to
634 define a synthetic minimal medium (Yus et al., 2009). This strategy of reverse ecology
635 implicitly validates that genomic information and reconstructed networks can guide the
636 formulation of culture media for other fastidious or uncultured bacteria (Cross et al., 2019;
637 Lewis et al., 2021). Under strictly defined conditions, the use of sugars or any other substrates
638 that do not directly feed the TCA cycle would theoretically require the addition of a TCA
639 intermediate. However, in empirical in vitro conditions, intracellular metabolite pools may
640 partially compensate for this requirement, as cells are not metabolically empty at the beginning

641 of the experiment. In natural environments, on the other hand, the chemical diversity
642 accessible to the bacterium would compensate for this metabolic obstacle. Interestingly,
643 minimal media tested in this study supported biofilm formation, with no significant differences
644 compared to the standard media PD3. *X. fastidiosa* is known to colonize xylem vessels
645 primarily in the form of biofilms, which play a key role in its pathogenicity (Marques et al.,
646 2002). This approach aimed to explore whether minimal environmental conditions, such as in
647 the xylem sap, could trigger biofilm development independently of an optimal planktonic
648 growth.

649 One of the most notable findings of this work is the first direct experimental evidence of
650 polyamine production in *X. fastidiosa*. Polyamines are well-established modulators of biofilm
651 formation and adhesion in many bacterial pathogens. They influence biofilm development
652 through effects on gene regulation, signaling pathways, and extracellular matrix production.
653 However, until now there was no direct experimental evidence of polyamines production by *X.*
654 *fastidiosa*. A previous study in citrus trees infected with this phytopathogen reported high
655 levels of putrescine (Purcino et al., 2007), although this observation was interpreted as a
656 stress signalling response by the plant host (Blázquez, 2024). In other phytopathogens, such
657 as *R. solanacearum* and *P. syringae,* polyamines have been considered as a virulence factor
658 (Lowe-Power et al., 2018; Solmi et al., 2025). In these pathogens, polyamines likely protect
659 bacteria against oxidative stress generated by plant defense responses and may contribute to
660 symptom development during infection.

661 Metabolic modelling has previously been used to explore production of virulence-associated
662 processes in plant pathogens. Other reconstructions of *X. fastidiosa* metabolism (Gerlin et al.,
663 2020; Oliveira et al., 2023) considered the secretion of two known virulence factors: the LesA
664 protein (Nascimento et al., 2016) and exopolysaccharides (EPS) (da Silva et al., 2001). The
665 metabolic model of *R. solanacearum* (Peyraud et al., 2016), also included polyamine
666 secretion. We extended this concept by exploring the relationship between polyamine
667 production and other virulence-associated factors in *X. fastidiosa*, namely LesA and EPS.

668 In this work, both metabolic modelling and experimental analyses indicated that *X. fastidiosa*
669 is capable of producing and secreting polyamines. Our simulations revealed a trade-off
670 between biomass growth, polyamine biosynthesis, and the production of other virulence
671 factors, suggesting that the synthesis of these compounds is metabolically constrained in this
672 bacterium. Spermidine and spermine production appear to be metabolically coupled due to
673 their dependence on shared precursors. Additionally, the simulations revealed a trade-off
674 between biomass production and the secretion of virulence factors. For instance, spermidine

and spermine production appeared to be more compatible with the secretion of LesA and EPS across a broader range of similar biomass levels.

Our experimental data, despite the variability typically observed when working with fastidious bacteria in vitro, showed a higher accumulation of spermidine in the culture supernatant. Additionally, polyamine levels tended to be higher in biofilms than in planktonic cells, suggesting a link between polyamine production and the biofilm state of this phytopathogen. While polyamines are established regulators of bacterial biofilms (Karatan & Michael, 2013) in *X. fastidiosa* this role remains untested experimentally. Current investigations in *X. fastidiosa* focus on EPS composition or processing (Janissen et al., 2015; Castro et al., 2023), the role of surface adhesins and pili (Scala et al., 2025), or of DSF-family quorum sensing signals (Horgan et al., 2024), without an explicit link to polyamine metabolism or signalling. Our results open the possibility that polyamines could represent an additional virulence factor in *X. fastidiosa*. Further in vivo studies will be necessary to determine to which extension bacterial metabolism is responsible of the polyamines detected in infected plants, and to clarify their role during host colonization by this species.

5. Conclusions

This work presents the first pangenome-based metabolic reconstruction for *X. fastidiosa*, integrating the conserved metabolic features shared across five subspecies of this plant pathogen. Following experimental validation, the iXfcore model successfully predicted minimal nutritional requirements, which were then used to design defined media capable of supporting biofilm formation in vitro. This outcome provided additional support for the model's predictive accuracy. The model also revealed a previously undescribed pathway for incorporating acetate into biomass precursors. In addition, simulations predicted that *X. fastidiosa* can overproduce polyamines—a finding that was later confirmed experimentally, providing the first in vitro evidence of polyamine production in this pathogen. Beyond these specific findings, the iXfcore model establishes a robust systems-level framework for building strain-specific metabolic models. This framework can be used to further explore the metabolism of *X. fastidiosa*, generate new hypotheses about its physiology and virulence mechanisms, and support future studies that integrate bacterial and plant metabolism to better understand host–pathogen interactions.

Funding sources

P.C.-A. was recipient of a predoctoral fellowship from the Generalitat Valenciana "Subvenciones para la contratación de personal investigador de carácter predoctoral (ACIF)", with reference ACIF/2021/110. M.Á.-H. was supported by the Generalitat Valenciana and the European Social Fund "ESF Investing in your future" through grant CIACIF/2022/333. J.P. acknowledges the generic support of CYTED (Iber-Xyfas network "Red Iberoamericana para la vigilancia de *Xylella fastidiosa*", ref. 119RT0569) as well as of his host institutions Universitat de València and CSIC. This work was financed by the HORIZON-CL6-2021-FARM2FORK-01 project BeXyl (Beyond *Xylella*, Integrated Management Strategies for Mitigating *Xylella fastidiosa* impact in Europe; Grant ID No 101060593). The funders had no role in study design, data collection and analysis, decision to publish, or presentation of the manuscript.

CRediT authorship contribution statement

Paola Corbín Agustí: Conceptualization, Methodology, Formal analysis, Visualization, Investigation, Software, Data curation, Writing– Original draft, Reviewing and Editing. **Miguel Álvarez Herrera**: Methodology, Formal analysis, Visualization, Investigation, Software, Writing– Reviewing and editing. **Miguel Román Écija**: Methodology, Formal analysis, Investigation, Writing– Reviewing and editing. **Patricia Álvarez**: Methodology, Investigation, Software, Writing– Reviewing and editing. **Marta Tortajada**: Conceptualization, Writing– Reviewing and editing. **Juli Peretó**: Conceptualization, Supervision, Funding acquisition, Writing– Original draft, Reviewing and Editing. **Blanca B. Landa**: Conceptualization, Supervision, Funding acquisition, Writing– Original draft, Reviewing and Editing.

Declaration of Competing Interest

M. Tortajada is a former employee of Biopolis-Archer Daniels Midland and contributed to this study in their personal capacity. The authors declare no conflicts of interest.

Data Availability

The code and data for reproducing this analysis are available in the Zenodo repository: https://doi.org/10.5281/zenodo.17307291

Acknowledgements

The authors thank the expert support of Miguel Ángel Blázquez and Francisco Vera-Sirera (IBMCP, UPV-CSIC) and the IBMCP Metabolomics Facility for the polyamine analyses. The authors thank Gonzalo de Oyanguren for the initial steps into the pangenome analysis. Figures 1C and 3 were created in BioRender. Smith, J. (2025).

Appendix A. Supplementary material

Supplementary Figures and Tables

PDF document containing supplementary figures and tables referred in the main text.

Supplementary Methods

PDF document describing metabolic model refinement and curation, additional in silico constraints and simulation conditions, and phenotypic characterization of *X. fastidiosa* strains.

Supplementary Results and Discussion

PDF document describing additional metabolic features of the iXfcore model, phenotypic characterization of *X. fastidiosa* strains, and the proposed pathway for acetate assimilation.

Supplementary Material 1 (SM1). iXfcore metabolic model.

Compressed archive (.zip) containing the model in SBML (.xml), JSON (.json), and MATLAB (.mat) formats.

Supplementary Material 2 (SM2). MEMOTE report for iXfcore.

HTML report detailing the results of the memote test suite, including network consistency, annotation coverage for metabolites, reactions, genes, and SBO terms and total score.

Supplementary Material 3 (SM3). Flux distribution in minimal medium with glutamine as carbon and nitrogen source.

Excel file reporting FBA and pFBA flux distributions ($mmol \cdot gDW^{-1} \cdot h^{-1}$) across reactions under the simulated minimal medium conditions.

Supplementary Material 4 (SM4). Defined minimal media results.

Excel file including in silico minimal media prediction and experimental measurements of growth and biofilm formation across the six designed synthetic minimal media.

Supplementary Material 5 (SM5). Flux distribution under acetate as sole carbon source.

Excel file reporting FBA and pFBA flux distributions ($mmol \cdot gDW^{-1} \cdot h^{-1}$) across reactions under acetate growth conditions.

Supplementary Material 6 (SM6). Polyamine experimental data.
Excel file containing experimental quantification of putrescine, spermidine, and spermine across the two different experiments.

Supplementary Material 7 (SM7). Phenotypic Biolog growth data.
Excel file containing PM1 and PM2 sAUGPC values, normalized data, and growth classification across the tested carbon sources.

Supplementary Material 8 (SM8). In silico growth predictions.
Excel file reporting FBA-predicted optimal growth fluxes ($mmol \cdot gDW^{-1} \cdot h^{-1}$) for the evaluated carbon sources.

References

Anguita-Maeso, M., Haro, C., Montes-Borrego, M., Fuente, L. D. L., Navas-Cortés, J. A., & Landa, B. B. (2021). Metabolomic, ionomic and microbial characterization of olive xylem sap reveals differences according to plant age and genotype. *Agronomy*, *11*(6). https://doi.org/10.3390/agronomy11061179

Ardalani, O., Phaneuf, P. V., Mohite, O. S., Nielsen, L. K., & Palsson, B. O. (2024). Pangenome reconstruction of *Lactobacillaceae* metabolism predicts species-specific metabolic traits. *mSystems*, *9*(7), e00156-24. https://doi.org/10.1128/msystems.00156-24

Blázquez, M. A. (2024). Polyamines: their role in plant development and stress. *Annual Review of Plant Biology*, *75*(Volume 75, 2024), 95–117. https://doi.org/10.1146/annurev-arplant-070623-110056

Brämer, C. O., & Steinbüchel, A. (2001). The methylcitric acid pathway in *Ralstonia eutropha*: New genes identified involved in propionate metabolism. *Microbiology*, *147*(8), 2203–2214. https://doi.org/10.1099/00221287-147-8-2203

Brock, M., Maerker, C., Schütz, A., Völker, U., & Buckel, W. (2002). Oxidation of propionate to pyruvate in *Escherichia coli*: Involvement of methylcitrate dehydratase and aconitase. *European Journal of Biochemistry*, *269*(24), 6184–6194. https://doi.org/10.1046/j.1432-1033.2002.03336.x

Camacho, C., Coulouris, G., Avagyan, V., Ma, N., Papadopoulos, J., Bealer, K., & Madden, T. L. (2009). BLAST+: Architecture and applications. *BMC Bioinformatics*, *10*(1), 421. https://doi.org/10.1186/1471-2105-10-421

Campanharo, J. C., Lemos, M. V. F., & Lemos, E. G. de M. (2003). Growth optimization procedures for the phytopathogen *Xylella fastidiosa*. *Current Microbiology*, *46*(2), 0099–0102. https://doi.org/10.1007/s00284-002-3829-z

Castro, C., Ndukwe, I., Heiss, C., Black, I., Ingel, B. M., Guevara, M., Sun, Y., Azadi, P., Sun, Q., & Roper, M. C. (2023). *Xylella fastidiosa* modulates exopolysaccharide polymer length and the dynamics of biofilm development with a β-1,4-endoglucanase. *mBio*, *14*(5), e01395-23. https://doi.org/10.1128/mbio.01395-23

Chang, C. J. (1993). *Xylella fastidiosa*: Cultivation in chemically defined medium. *Phytopathology*, *83*(2), 192. https://doi.org/10.1094/Phyto-83-192

Chatterjee, S., Almeida, R. P. P., & Lindow, S. (2008). Living in two worlds: the plant and insect lifestyles of *Xylella fastidiosa. Annual Review of Phytopathology*, *46*(1), 243–271. https://doi.org/10.1146/annurev.phyto.45.062806.094342

Chavarría, M., Nikel, P. I., Pérez-Pantoja, D., & de Lorenzo, V. (2013). The Entner-Doudoroff pathway empowers *Pseudomonas putida* KT2440 with a high tolerance to oxidative

stress. *Environmental Microbiology*, *15*(6), 1772–1785. https://doi.org/10.1111/1462-2920.12069

Cross, K. L., Campbell, J. H., Balachandran, M., Campbell, A. G., Cooper, C. J., Griffen, A., Heaton, M., Joshi, S., Klingeman, D., Leys, E., Yang, Z., Parks, J. M., & Podar, M. (2019). Targeted isolation and cultivation of uncultivated bacteria by reverse genomics. *Nature Biotechnology*, *37*(11), 1314–1321. https://doi.org/10.1038/s41587-019-0260-6

da Silva, F. R., Vettore, A. L., Kemper, E. L., Leite, A., & Arruda, P. (2001). Fastidian gum: The *Xylella fastidiosa* exopolysaccharide possibly involved in bacterial pathogenicity. *FEMS Microbiology Letters*, *203*(2), 165–171. https://doi.org/10.1111/j.1574-6968.2001.tb10836.x

Davis, M. J. (1992). Fastidious bacteria of plant vascular tissues and their invertebrate vectors. In *The Prokaryotes* (pp. 4030–4049). *Springer*. https://doi.org/10.1007/978-1-4757-2191-1_66

Davis, M. J., French, W. J., & Schaad, N. W. (1981). Axenic culture of the bacteria associated with phony disease of peach and plum leaf scald. *Current Microbiology*, *6*(5), 309–314. https://doi.org/10.1007/BF01566883

Davis, M. J., Gillaspie, A. G., Harris, R. W., & Lawson, R. H. (1980). Ratoon Stunting Disease of Sugarcane: Isolation of the Causal Bacterium. *Science*, *210*(4476), 1365–1367. https://doi.org/10.1126/science.210.4476.1365

De La Fuente, L., Navas-Cortés, J. A., & Landa, B. B. (2024). Ten challenges to understanding and managing the insect-transmitted, xylem-limited bacterial pathogen *Xylella fastidiosa*. *Phytopathology*, *114*(5), 869–884. https://doi.org/10.1094/PHYTO-12-23-0476-KC

de Macedo Lemos, E. G., Alves, L. M. C., & Campanharo, J. C. (2003). Genomics-based design of defined growth media for the plant pathogen *Xylella fastidiosa*. *FEMS Microbiology Letters*, *219*(1), 39–45. https://doi.org/10.1016/S0378-1097(02)01189-8

Denancé, N., Briand, M., Gaborieau, R., Gaillard, S., & Jacques, M.-A. (2019). Identification of genetic relationships and subspecies signatures in *Xylella fastidiosa*. *BMC Genomics*, *20*(1), 239. https://doi.org/10.1186/s12864-019-5565-9

Dolan, S. K., Wijaya, A., Geddis, S. M., Spring, D. R., Silva-Rocha, R., & Welch, M. (2018). Loving the poison: The methylcitrate cycle and bacterial pathogenesis. *Microbiology*, *164*(3), 251–259. https://doi.org/10.1099/mic.0.000604

Ebrahim, A., Lerman, J. A., Palsson, B. O., & Hyduke, D. R. (2013). COBRApy: COnstraints-Based Reconstruction and Analysis for Python. *BMC Systems Biology*, *7*(1), 74. https://doi.org/10.1186/1752-0509-7-74

EFSA (European Food Safety Authority), E. F. S., Cavalieri, V., Fasanelli, E., Furnari, G., Gibin, D., Gutierrez Linares, A., La Notte, P., Pasinato, L., & Stancanelli, G. (2026). Update of the *Xylella* spp. Host plant database – Systematic literature search up to 30 June 2025. *EFSA Journal*, *24*(1), e9840. https://doi.org/10.2903/j.efsa.2026.9840

EPPO (2023) PM 7/24 (5) *Xylella fastidiosa*. *EPPO Bulletin*, *53*(2), 205–276. https://doi.org/10.1111/epp.12923

Erb, T. J., Berg, I. A., Brecht, V., Müller, M., Fuchs, G., & Alber, B. E. (2007). Synthesis of C_5 -dicarboxylic acids from C_2 -units involving crotonyl-CoA carboxylase/reductase: The ethylmalonyl-CoA pathway. *Proceedings of the National Academy of Sciences*, *104*(25), 10631–10636. https://doi.org/10.1073/pnas.0702791104

Gerlin, L., Cottret, L., Cesbron, S., Taghouti, G., Jacques, M.-A., Genin, S., & Baroukh, C. (2020). Genome-scale investigation of the metabolic determinants generating bacterial fastidious growth. *mSystems*, *5*(2), 10.1128/msystems.00698-19. https://doi.org/10.1128/msystems.00698-19

Gil, R., & Peretó, J. (2015). Small genomes and the difficulty to define minimal translation and metabolic machineries. *Frontiers in Ecology and Evolution*, *3*. https://doi.org/10.3389/fevo.2015.00123

Gu, C., Kim, G. B., Kim, W. J., Kim, H. U., & Lee, S. Y. (2019). Current status and applications of genome-scale metabolic models. *Genome Biology*, *20*(1), 121. https://doi.org/10.1186/s13059-019-1730-3

Hagberg, A., Swart, P. J., & Schult, D. A. (2008). Exploring network structure, dynamics, and function using NetworkX. In G. Varoquaux, T. Vaught, & J. Millman (Eds.), *Proceedings of the 7th Python in Science Conference (SciPy2008)* (pp. 11–15).

Hanage, W. P., Fraser, C., & Spratt, B. G. (2005). Fuzzy species among recombinogenic bacteria. *BMC Biology*, *3*(1), 6. https://doi.org/10.1186/1741-7007-3-6

Henry, C. S., DeJongh, M., Best, A. A., Frybarger, P. M., Linsay, B., & Stevens, R. L. (2010). High-throughput generation, optimization and analysis of genome-scale metabolic models. *Nature Biotechnology*, *28*(9), 977–982. https://doi.org/10.1038/nbt.1672

Herter, S., Fuchs, G., Bacher, A., & Eisenreich, W. (2002). A bicyclic autotrophic CO2 fixation pathway in *Chloroflexus aurantiacus*. *Journal of Biological Chemistry*, *277*(23), 20277–20283. https://doi.org/10.1074/jbc.M201030200

Hiery, E., Adam, S., Reid, S., Hofmann, J., Sonnewald, S., & Burkovski, A. (2013). Genome-wide transcriptome analysis of *Clavibacter michiganensis* subsp. *michiganensis* grown in xylem mimicking medium. *Journal of Biotechnology*, *168*(4), 348–354. https://doi.org/10.1016/j.jbiotec.2013.09.006

Horgan, C., Baccari, C., O'Driscoll, M., Lindow, S. E., & O'Sullivan, T. P. (2024). BDSF

888 analogues inhibit quorum sensing-regulated biofilm production in *Xylella fastidiosa*.
889 *Microorganisms*, *12*(12), 2496. https://doi.org/10.3390/microorganisms12122496
890 Ibarra, R. U., Edwards, J. S., & Palsson, B. O. (2002). *Escherichia coli* K-12 undergoes
891 adaptive evolution to achieve in silico predicted optimal growth. *Nature*, *420*(6912),
892 186–189. https://doi.org/10.1038/nature01149
893 Igarashi, K., & Kashiwagi, K. (2010). Characteristics of cellular polyamine transport in
894 prokaryotes and eukaryotes. *Plant Physiology and Biochemistry: PPB*, *48*(7), 506–
895 512. https://doi.org/10.1016/j.plaphy.2010.01.017
896 Janissen, R., Murillo, D. M., Niza, B., Sahoo, P. K., Nobrega, M. M., Cesar, C. L., Temperini,
897 M. L. A., Carvalho, H. F., De Souza, A. A., & Cotta, M. A. (2015). Spatiotemporal
898 distribution of different extracellular polymeric substances and filamentation mediate
899 *Xylella fastidiosa* adhesion and biofilm formation. *Scientific Reports*, *5*(1), 9856.
900 https://doi.org/10.1038/srep09856
901 Jolley, K. A., Bray, J. E., & Maiden, M. C. J. (2018). Open-access bacterial population
902 genomics: BIGSdb software, the PubMLST.org website and their applications.
903 *Wellcome Open Research*, *3*, 124. https://doi.org/10.12688/wellcomeopenres.14826.1
904 Kanehisa, M., Sato, Y., & Morishima, K. (2016). BlastKOALA and GhostKOALA: KEGG Tools
905 for functional characterization of genome and metagenome sequences. *Journal of*
906 *Molecular Biology*, *428*(4), 726–731. https://doi.org/10.1016/j.jmb.2015.11.006
907 Karatan, E., & Michael, A. J. (2013). A wider role for polyamines in biofilm formation.
908 *Biotechnology Letters*, *35*(11), 1715–1717. https://doi.org/10.1007/s10529-013-1286-
909 3
910 Khomyakova, M., Bükmez, Ö., Thomas, L. K., Erb, T. J., & Berg, I. A. (2011). A
911 methylaspartate cycle in Haloarchaea. *Science*, *331*(6015), 334–337.
912 https://doi.org/10.1126/science.1196544
913 Kim, J., Kershner, J. P., Novikov, Y., Shoemaker, R. K., & Copley, S. D. (2010). Three
914 serendipitous pathways in *E. coli* can bypass a block in pyridoxal-5'-phosphate
915 synthesis. *Molecular Systems Biology*, *6*, 436. https://doi.org/10.1038/msb.2010.88
916 King, Z. A., Dräger, A., Ebrahim, A., Sonnenschein, N., Lewis, N. E., & Palsson, B. O. (2015).
917 Escher: A web application for building, sharing, and embedding data-rich visualizations
918 of biological pathways. *PLOS Computational Biology*, *11*(8), e1004321.
919 https://doi.org/10.1371/journal.pcbi.1004321
920 King, Z. A., Lu, J., Dräger, A., Miller, P., Federowicz, S., Lerman, J. A., Ebrahim, A., Palsson,
921 B. O., & Lewis, N. E. (2016). BiGG Models: A platform for integrating, standardizing
922 and sharing genome-scale models. *Nucleic Acids Research*, *44*(D1), D515–D522.
923 https://doi.org/10.1093/nar/gkv1049

Kornberg, H. L., & Krebs, H. A. (1957). Synthesis of cell constituents from C2-units by a modified tricarboxylic acid cycle. *Nature*, *179*(4568), 988–991. https://doi.org/10.1038/179988a0

Kremer, K., Van Teeseling, M. C. F., Schada Von Borzyskowski, L., Bernhardsgrütter, I., Van Spanning, R. J. M., Gates, A. J., Remus-Emsermann, M. N. P., Thanbichler, M., & Erb, T. J. (2019). Dynamic metabolic rewiring enables efficient acetyl coenzyme a assimilation in *Paracoccus denitrificans*. *mBio*, *10*(4), e00805-19. https://doi.org/10.1128/mBio.00805-19

Landa, B. B., Castillo, A. I., Giampetruzzi, A., Kahn, A., Román-Écija, M., Velasco-Amo, M. P., Navas-Cortés, J. A., Marco-Noales, E., Barbé, S., Moralejo, E., Coletta-Filho, H. D., Saldarelli, P., Saponari, M., & Almeida, R. P. P. (2020). Emergence of a plant pathogen in Europe associated with multiple intercontinental introductions. *Applied and Environmental Microbiology*, *86*(3), e01521-19. https://doi.org/10.1128/AEM.01521-19

Landa, B. B., Saponari, M., Feitosa-Junior, O. R., Giampetruzzi, A., Vieira, F. J. D., Mor, E., & Robatzek, S. (2022). *Xylella fastidiosa* 's relationships: The bacterium, the host plants, and the plant microbiome. *New Phytologist*, *234*(5), 1598–1605. https://doi.org/10.1111/nph.18089

Leite, B., Andersen, P. C., & Ishida, M. L. (2004). Colony aggregation and biofilm formation in xylem chemistry-based media for *Xylella fastidiosa*. *FEMS Microbiology Letters*, *230*(2), 283–290. https://doi.org/10.1016/S0378-1097(03)00917-0

Lewis, W. H., Tahon, G., Geesink, P., Sousa, D. Z., & Ettema, T. J. G. (2021). Innovations to culturing the uncultured microbial majority. *Nature Reviews Microbiology*, *19*(4), 225–240. https://doi.org/10.1038/s41579-020-00458-8

Lieven, C., Beber, M. E., Olivier, B. G., Bergmann, F. T., Ataman, M., Babaei, P., Bartell, J. A., Blank, L. M., Chauhan, S., Correia, K., Diener, C., Dräger, A., Ebert, B. E., Edirisinghe, J. N., Faria, J. P., Feist, A. M., Fengos, G., Fleming, R. M. T., García-Jiménez, B., … Zhang, C. (2020). MEMOTE for standardized genome-scale metabolic model testing. *Nature Biotechnology*, *38*(3), 272–276. https://doi.org/10.1038/s41587-020-0446-y

Lowe-Power, T. M., Hendrich, C. G., Von Roepenack-Lahaye, E., Li, B., Wu, D., Mitra, R., Dalsing, B. L., Ricca, P., Naidoo, J., Cook, D., Jancewicz, A., Masson, P., Thomma, B., Lahaye, T., Michael, A. J., & Allen, C. (2018). Metabolomics of tomato xylem sap during bacterial wilt reveals *Ralstonia solanacearum* produces abundant putrescine, a metabolite that accelerates wilt disease. *Environmental Microbiology*, *20*(4), 1330–1349. https://doi.org/10.1111/1462-2920.14020

Lv, P., Tang, W., Wang, P., Cao, Z., & Zhu, G. (2018). Enzymatic characterization and functional implication of two structurally different isocitrate dehydrogenases from *Xylella fastidiosa*. *Biotechnology and Applied Biochemistry*, *65*(2), 230–237. https://doi.org/10.1002/bab.1560

Madeira, F., Madhusoodanan, N., Lee, J., Eusebi, A., Niewielska, A., Tivey, A. R. N., Lopez, R., & Butcher, S. (2024). The EMBL-EBI Job Dispatcher sequence analysis tools framework in 2024. *Nucleic Acids Research*, *52*(W1), W521–W525. https://doi.org/10.1093/nar/gkae241

Malik-Sheriff, R. S., Glont, M., Nguyen, T. V. N., Tiwari, K., Roberts, M. G., Xavier, A., Vu, M. T., Men, J., Maire, M., Kananathan, S., Fairbanks, E. L., Meyer, J. P., Arankalle, C., Varusai, T. M., Knight-Schrijver, V., Li, L., Dueñas-Roca, C., Dass, G., Keating, S. M., … Hermjakob, H. (2020). BioModels—15 years of sharing computational models in life science. *Nucleic Acids Research*, *48*(D1), D407–D415. https://doi.org/10.1093/nar/gkz1055

Marques, L. L. R., Ceri, H., Manfio, G. P., Reid, D. M., & Olson, M. E. (2002). Characterization of biofilm formation by *Xylella fastidiosa* in vitro. *Plant Disease*, *86*(6), 633–638. https://doi.org/10.1094/PDIS.2002.86.6.633

Mirhakkak, M. H., Chen, X., Ni, Y., Heinekamp, T., Sae-Ong, T., Xu, L.-L., Kurzai, O., Barber, A. E., Brakhage, A. A., Boutin, S., Schäuble, S., & Panagiotou, G. (2023). Genome-scale metabolic modeling of *Aspergillus fumigatus* strains reveals growth dependencies on the lung microbiome. *Nature Communications*, *14*(1), 4369. https://doi.org/10.1038/s41467-023-39982-5

Monk, J., Nogales, J., & Palsson, B. O. (2014). Optimizing genome-scale network reconstructions. *Nature Biotechnology*, *32*(5), 447–452. https://doi.org/10.1038/nbt.2870

Nascimento, R., Gouran, H., Chakraborty, S., Gillespie, H. W., Almeida-Souza, H. O., Tu, A., Rao, B. J., Feldstein, P. A., Bruening, G., Goulart, L. R., & Dandekar, A. M. (2016). The type II secreted lipase/esterase LesA is a key virulence factor required for *Xylella fastidiosa* pathogenesis in grapevines. *Scientific Reports*, *6*(1), 18598. https://doi.org/10.1038/srep18598

Neumann, M. (2003). Sequence tag analysis of gene expression during pathogenic growth and microsclerotia development in the vascular wilt pathogen *Verticillium dahliae*. *Fungal Genetics and Biology*, *38*(1), 54–62. https://doi.org/10.1016/S1087-1845(02)00507-8

Nogales, J. (2017). A practical protocol for genome-scale metabolic reconstructions. In T. J. McGenity, K. N. Timmis, & B. Nogales (Eds), *Hydrocarbon and lipid microbiology*

protocols: genetic, genomic and system analyses of pure cultures (pp. 197–221). Springer. https://doi.org/10.1007/8623_2014_12

Norsigian, C. J., Fang, X., Seif, Y., Monk, J. M., & Palsson, B. O. (2020). A workflow for generating multi-strain genome-scale metabolic models of prokaryotes. *Nature Protocols*, *15*(1), 1–14. https://doi.org/10.1038/s41596-019-0254-3

O'Brien, E. J., Monk, J. M., & Palsson, B. O. (2015). Using genome-scale models to predict biological capabilities. *Cell*, *161*(5), 971–987. https://doi.org/10.1016/j.cell.2015.05.019

Oliveira, A., Cunha, E., Silva, M., Faria, C., & Dias, O. (2023). Exploring *Xylella fastidiosa*'s metabolic traits using a GSM model of the phytopathogenic bacterium. In F. Fdez-Riverola, M. Rocha, M. S. Mohamad, S. Caraiman, & A. B. Gil-González (Eds), *Practical Applications of Computational Biology and Bioinformatics, 16th International Conference (PACBB 2022)* (Vol. 553, pp. 79–88). Springer International Publishing. https://doi.org/10.1007/978-3-031-17024-9_8

Orth, J. D., Conrad, T. M., Na, J., Lerman, J. A., Nam, H., Feist, A. M., & Palsson, B. Ø. (2011). A comprehensive genome-scale reconstruction of *Escherichia coli* metabolism—2011. *Molecular Systems Biology*, *7*(1), 535. https://doi.org/10.1038/msb.2011.65

Orth, J. D., Thiele, I., & Palsson, B. Ø. (2010). What is flux balance analysis? *Nature Biotechnology*, *28*(3), 245–248. https://doi.org/10.1038/nbt.1614

Overbeek, R., Begley, T., Butler, R. M., Choudhuri, J. V., Chuang, H.-Y., Cohoon, M., de Crécy-Lagard, V., Diaz, N., Disz, T., Edwards, R., Fonstein, M., Frank, E. D., Gerdes, S., Glass, E. M., Goesmann, A., Hanson, A., Iwata-Reuyl, D., Jensen, R., Jamshidi, N., … Vonstein, V. (2005). The subsystems approach to genome annotation and its use in the project to annotate 1000 genomes. *Nucleic Acids Research*, *33*(17), 5691–5702. https://doi.org/10.1093/nar/gki866

Palsson, B. Ø. (2015). *Systems Biology: Constraint-based reconstruction and analysis*. Cambridge University Press. https://doi.org/10.1017/CBO9781139854610

Peyraud, R., Cottret, L., Marmiesse, L., Gouzy, J., & Genin, S. (2016). A Resource Allocation Trade-Off between Virulence and Proliferation Drives Metabolic Versatility in the Plant Pathogen Ralstonia solanacearum. *PLOS Pathogens*, *12*(10), e1005939. https://doi.org/10.1371/journal.ppat.1005939

Purcino, R. P., Medina, C. L., Martins de Souza, D., Winck, F. V., Machado, E. C., Novello, J. C., Machado, M. A., & Mazzafera, P. (2007). *Xylella fastidiosa* disturbs nitrogen metabolism and causes a stress response in sweet orange *Citrus sinensis* cv. Pera. *Journal of Experimental Botany*, *58*(11), 2733–2744. https://doi.org/10.1093/jxb/erm138

Qian, J., & Ye, C. (2024). Development and applications of genome-scale metabolic network models. In *Advances in Applied Microbiology* (Vol. 126, pp. 1–26). Academic Press. https://doi.org/10.1016/bs.aambs.2024.02.002

Remm, M., Storm, C. E. V., & Sonnhammer, E. L. L. (2001). Automatic clustering of orthologs and in-paralogs from pairwise species comparisons. *Journal of Molecular Biology*, *314*(5), 1041–1052. https://doi.org/10.1006/jmbi.2000.5197

Román-Écija, M., Navas-Cortés, J. A., Velasco-Amo, M. P., Arias-Giraldo, L. F., Gómez, L. M., Fuente, L. D. L., & Landa, B. B. (2023). Two *Xylella fastidiosa* subsp. *multiplex* strains isolated from almond in spain differ in plasmid content and virulence traits. *Phytopathology*, *113*(6), 960–974. https://doi.org/10.1094/PHYTO-06-22-0234-R

Sanchez, F. B., Barreiro, H. J., Soto, E. I., & Rodriguez, C. E. (2019). *The Impact Indicator for Priority Pests (I2P2): A tool for ranking pests according to Regulation (EU) 2016/2031*. Publications Office of the European Union. https://doi.org/10.2760/585182

Santos, A. P., Muratore, L. N., Solé-Gil, A., Farías, M. E., Ferrando, A., Blázquez, M. A., & Belfiore, C. (2021). Extremophilic bacteria restrict the growth of *Macrophomina phaseolina* by combined secretion of polyamines and lytic enzymes. *Biotechnology Reports*, *32*, e00674. https://doi.org/10.1016/j.btre.2021.e00674

Sayers, E. W., Beck, J., Bolton, E. E., Brister, J. R., Chan, J., Connor, R., Feldgarden, M., Fine, A. M., Funk, K., Hoffman, J., Kannan, S., Kelly, C., Klimke, W., Kim, S., Lathrop, S., Marchler-Bauer, A., Murphy, T. D., O'Sullivan, C., Schmieder, E., … Pruitt, K. D. (2024). Database resources of the National Center for Biotechnology Information in 2025. *Nucleic Acids Research*, *53*(D1), D20–D29. https://doi.org/10.1093/nar/gkae979

Scala, V., Salustri, M., Merfa, M. V., Beccaccioli, M., Lascala, L., De La Fuente, L., & Reverberi, M. (2025). XadA-like adhesin XADA2 regulates biofilm formation in *X. fastidiosa* subsp. *fastidiosa* putatively by engaging oleic-acid derived oxylipins. *Molecular Biology Reports*, *52*(1), 263. https://doi.org/10.1007/s11033-025-10259-y

Scally, M., Schuenzel, E. L., Stouthamer, R., & Nunney, L. (2005). Multilocus sequence type system for the plant pathogen *Xylella fastidiosa* and relative contributions of recombination and point mutation to clonal diversity. *Applied and Environmental Microbiology*, *71*(12), 8491–8499. https://doi.org/10.1128/AEM.71.12.8491-8499.2005

Schada von Borzyskowski, L., Bernhardsgrütter, I., & Erb, T. J. (2020). Biochemical unity revisited: Microbial central carbon metabolism holds new discoveries, multi-tasking pathways, and redundancies with a reason. *Biological Chemistry*, *401*(12), 1429–1441. https://doi.org/10.1515/hsz-2020-0214

Schatschneider, S., Persicke, M., Watt, S. A., Hublik, G., Pühler, A., Niehaus, K., & Vorhölter, F.-J. (2013). Establishment, in silico analysis, and experimental verification of a large-

scale metabolic network of the xanthan producing *Xanthomonas campestris* pv. campestris strain B100. *Journal of Biotechnology*, *167*(2), 123–134. https://doi.org/10.1016/j.jbiotec.2013.01.023

Segura, D., Mahadevan, R., Juárez, K., & Lovley, D. R. (2008). Computational and experimental analysis of redundancy in the central metabolism of *Geobacter sulfurreducens*. *PLOS Computational Biology*, *4*(2), e36. https://doi.org/10.1371/journal.pcbi.0040036

Shannon, P., Markiel, A., Ozier, O., Baliga, N. S., Wang, J. T., Ramage, D., Amin, N., Schwikowski, B., & Ideker, T. (2003). Cytoscape: A software environment for integrated models of biomolecular interaction networks. *Genome Research*, *13*(11), 2498–2504. https://doi.org/10.1101/gr.1239303

Simko, I., & Piepho, H.-P. (2012). The area under the disease progress stairs: Calculation, advantage, and application. *Phytopathology*, *102*(4), 381–389. https://doi.org/10.1094/PHYTO-07-11-0216

Simpson, A. J., Reinach, F. C., Arruda, P., Abreu, F. A., Acencio, M., Alvarenga, R., Alves, L. M., Araya, J. E., Baia, G. S., Baptista, C. S., Barros, M. H., Bonaccorsi, E. D., Bordin, S., Bové, J. M., Briones, M. R., Bueno, M. R., Camargo, A. A., Camargo, L. E., Carraro, D. M., … Setubal, J. C. (2000). The genome sequence of the plant pathogen *Xylella fastidiosa*. *Nature*, *406*(6792), 151–157. https://doi.org/10.1038/35018003

Solé-Gil, A., Hernández-García, J., López-Gresa, M. P., Blázquez, M. A., & Agustí, J. (2019). Conservation of thermospermine synthase activity in vascular and non-vascular plants. *Frontiers in Plant Science*, *10*. https://doi.org/10.3389/fpls.2019.00663

Solmi, L., Rossi, F. R., Romero, F. M., Bach-Pages, M., Preston, G. M., & Gárriz, A. (2025). The influence of the polyamine synthesis pathways on *Pseudomonas syringae* virulence and plant interaction. *Microbiology*, *171*(6), 001569. https://doi.org/10.1099/mic.0.001569

Sugiyama, Y., Nara, M., Sakanaka, M., Gotoh, A., Kitakata, A., Okuda, S., & Kurihara, S. (2017). Comprehensive analysis of polyamine transport and biosynthesis in the dominant human gut bacteria: Potential presence of novel polyamine metabolism and transport genes. *The International Journal of Biochemistry & Cell Biology*, *93*, 52–61. https://doi.org/10.1016/j.biocel.2017.10.015

Surano, A., del Grosso, C., Musio, B., Todisco, S., Giampetruzzi, A., Altamura, G., Saponari, M., Gallo, V., Mastrorilli, P., Boscia, D., & Saldarelli, P. (2024). Exploring the xylem-sap to unravel biological features of *Xylella fastidiosa* subspecies *pauca* ST53 in immune, resistant and susceptible crop species through metabolomics and in vitro studies. *Frontiers in Plant Science*, *14*. https://doi.org/10.3389/fpls.2023.1343876

Tabuchi, T., Serizawa, N., & Uchiyama, H. (1974). A novel pathway for the partial oxidation of propionyl-coa to pyruvate *via* seven-carbon tricarboxylic acids in yeasts. *Agricultural and Biological Chemistry*, *38*(12), 2571–2572. https://doi.org/10.1080/00021369.1974.10858334

Thiele, I., & Palsson, B. Ø. (2010). A protocol for generating a high-quality genome-scale metabolic reconstruction. *Nature Protocols*, *5*(1), 93–121. https://doi.org/10.1038/nprot.2009.203

UniProt Consortium. (2025). UniProt: The Universal Protein Knowledgebase in 2025. *Nucleic Acids Research*, *53*(D1), D609–D617. https://doi.org/10.1093/nar/gkae1010

Vanhove, M., Retchless, A. C., Sicard, A., Rieux, A., Coletta-Filho, H. D., De La Fuente, L., Stenger, D. C., & Almeida, R. P. P. (2019). Genomic diversity and recombination among *Xylella fastidiosa* subspecies. *Applied and Environmental Microbiology*, *85*(13), e02972-18. https://doi.org/10.1128/AEM.02972-18

Wang, P., Lee, Y., Igo, M. M., & Roper, M. C. (2017). Tolerance to oxidative stress is required for maximal xylem colonization by the xylem-limited bacterial phytopathogen, *Xylella fastidiosa*. *Molecular Plant Pathology*, *18*(7), 990–1000. https://doi.org/10.1111/mpp.12456

Wells, J. M., Raju, B. C., Hung, H.-Y., Weisburg, W. G., Mandelco-Paul, L., & Brenner, D. J. (1987). *Xylella fastidiosa* gen. nov., sp. nov: Gram-negative, xylem-limited, fastidious plant bacteria related to *Xanthomonas* spp. *International Journal of Systematic and Evolutionary Microbiology*, *37*(2), 136–143. https://doi.org/10.1099/00207713-37-2-136

Wells, J. M., Raju, B. C., Nyland, G., & Lowe, S. K. (1981). Medium for isolation and growth of bacteria associated with plum leaf scald and phony peach diseases. *Applied and Environmental Microbiology*, *42*(2), 357–363. https://doi.org/10.1128/aem.42.2.357-363.1981

Ye, C., Wei, X., Shi, T., Sun, X., Xu, N., Gao, C., & Zou, W. (2022). Genome-scale metabolic network models: From first-generation to next-generation. *Applied Microbiology and Biotechnology*, *106*(13), 4907–4920. https://doi.org/10.1007/s00253-022-12066-y

Youssefi, F., Brown, P., & Weinbaum, S. (2000). Relationship between tree nitrogen status, xylem and phloem sap amino acid concentrations, and apparent soil nitrogen uptake by almond trees *(Prunus dulcis)*. *The Journal of Horticultural Science and Biotechnology*, *75*(1), 62–68. https://doi.org/10.1080/14620316.2000.11511201

Yus, E., Maier, T., Michalodimitrakis, K., van Noort, V., Yamada, T., Chen, W.-H., Wodke, J. A. H., Güell, M., Martínez, S., Bourgeois, R., Kühner, S., Raineri, E., Letunic, I., Kalinina, O. V., Rode, M., Herrmann, R., Gutiérrez-Gallego, R., Russell, R. B., Gavin,

A.-C., … Serrano, L. (2009). Impact of genome reduction on bacterial metabolism and its regulation. *Science*, *326*(5957), 1263–1268. https://doi.org/10.1126/science.1177263

yWorks GmbH (2020). *yEd Graph Editor* (Version 3.18.2) [Computer software]. https://www.yworks.com/products/yed

Zarzycki, J., & Fuchs, G. (2011). Coassimilation of organic substrates via the autotrophic 3-hydroxypropionate bi-cycle in *Chloroflexus aurantiacus*. *Applied and Environmental Microbiology*, *77*(17), 6181–6188. https://doi.org/10.1128/AEM.00705-11

Zhu, G., Golding, G. B., & Dean, A. M. (2005). The selective cause of an ancient adaptation. *Science*, *307*(5713), 1279–1282. https://doi.org/10.1126/science.1106974

1150

1151 **Figure Legends**

1152

1153 **Figure 1. Genome-scale metabolic model reconstruction of *Xylella fastidiosa* through a**
1154 **pangenome based on the subspecies *pauca*, *multiplex*, *fastidiosa*, *morus* and *sandyi*.**
1155 A) Pangenome analysis illustrating the distribution of core genes, genes shared between
1156 subspecies and unique genes. Each bar in the vertical bar chart represents the number of
1157 ortholog groups shared by the strains indicated below the chart. B) Summary of the features
1158 (reactions, metabolites and genes) from the *X. fastidiosa* metabolic core (iXfcore)
1159 reconstructed in this work. For further information on accessory genes, see Supplementary
1160 Results and Discussion, and Table S2. C) Predicted flux distribution through the core
1161 metabolism, using FBA, in a minimal medium with glutamine as the sole carbon and nitrogen
1162 source, achieving a specific growth rate of 0.41 h^{-1}. Metabolic fluxes ($mmol \cdot gDW^{-1} \cdot h^{-1}$) are
1163 portrayed numerically.

1164

1165 **Figure 2. Evaluation of six synthetic defined growth media based on iXfcore model**
1166 **predictions**. Total bacterial growth measured by the standardized area under the growth
1167 progress curve (sAUGPC) (A) and biofilm formation (B) of seven *Xylella fastidiosa* strains grow
1168 at 28 °C for 6 days. PD3 medium is included as a positive control. Statistical differences
1169 between each synthetic defined medium and the PD3 control were assessed using Wilcoxon
1170 rank-sum tests. Significance levels of comparisons are displayed above each line connecting
1171 group pairs (ns: $P>0.05$, *: $P\leq0.05$, **: $P\leq0.01$, ***: $P\leq0.001$, ****: $P\leq0.0001$).

1172

1173 **Figure 3. Predicted acetate assimilation by the iXfcore model.** Flux distribution through
1174 the *Xylella fastidiosa* core metabolism, using FBA, in medium with acetate as the sole carbon
1175 and glutamic acid and ammonium as nitrogen source, achieving a specific growth rate of 1.14
1176 h^{-1}. Metabolic fluxes ($mmol \cdot gDW^{-1} \cdot h^{-1}$) are portrayed numerically. The alternative metabolic
1177 strategy for converting acetate into biomass combines two previously described modules: half
1178 of the 3-hydroxypropionate (3HP) bicycle (Herter et al., 2002) and the methylcitrate pathway
1179 (Brämer & Steinbüchel, 2001; Dolan et al., 2018) for propionyl-CoA assimilation. The enzymes
1180 and genes involved in the metabolic steps (1-11) of this pathway are in Supplementary Table
1181 S4. Abbreviations for metabolites participating in the 3HP pathway and the methylcitrate

1182 pathway: MCOA (malonyl CoA), MSA (malonate semialdehyde or 3-oxopropanoate), 3HP (3-
1183 hydroxypropionate), 3HPCOA (3-hrydroxypropionyl CoA), PP2COA (acryloyl CoA), PPCOA
1184 (propionyl CoA), 2MCIT (2-methylcitrate), 2MCACN (2-methylaconitate), MICT (2-
1185 methylisocitrate).

1186

1187 **Figure 4. Polyamine production by *Xylella fastidiosa.*** A) Trade-off between biomass and
1188 polyamine production using the iXfcore model. This figure illustrates the inverse relationship
1189 between growth (biomass accumulation) and the production of polyamines (putrescine,
1190 spermidine, and spermine) when one of the polyamines is completely absent. Simulations
1191 were performed using a minimal medium where glutamine served as the sole carbon source
1192 (with an uptake flux of 15.665 $mmol \cdot gDW^{-1} \cdot h^{-1}$). For each data point, the biomass reaction
1193 was maximized while the production fluxes for the polyamines (putrescine, spermidine, and
1194 spermine) were incrementally forced to the values represented by axis in flux units,
1195 $mmol \cdot gDW^{-1} \cdot h^{-1}$. A minimal threshold of 0.1608 $mmol \cdot gDW^{-1} \cdot h^{-1}$ was established for the
1196 consideration of growth. B) In vitro production of putrescine, spermidine and spermine across
1197 different sample types (cell pellet from biofilm, CP-B; cell pellet from planktonic growth, CP-P;
1198 and culture supernatant, SP). Samples were obtained from three *X. fastidiosa* strains (De
1199 Donno, ESVL and Temecula1) grown at 28 °C in PD3 medium for 5 and 12 days, with four
1200 replicates for each sample and time point. Concentrations (in $ng \cdot mL^{-1}$) are visualized with a
1201 pseudo-logarithmic scale. Statistical differences between time points within each sample type
1202 and strain were assessed using Wilcoxon rank-sum tests. Only significant results are indicated
1203 ($*$: $P \leq 0.05$).

1204

1205 **Figure 5. Trade-off between biomass and virulence factor production in *Xylella***
1206 ***fastidiosa.*** This figure illustrates the inverse relationship between growth (biomass
1207 accumulation) and the production of: LesA protein, fastidian gum EPS, and putrescine (A),
1208 spermidine (B) or spermine (C) using the iXfcore metabolic mode, when one of the three
1209 compounds is completely absent. Simulations were performed using a minimal medium where
1210 glutamine served as the sole carbon source (with an uptake flux of 15.664 $mmol \cdot gDW^{-1} \cdot h^{-1}$).
1211 For each data point, the biomass reaction was maximized while the production fluxes for the
1212 virulence factors (LesA, EPS, polyamine) were incrementally forced to the values represented
1213 by the axis in flux units, $mmol \cdot gDW^{-1} \cdot h^{-1}$. A minimal threshold of 0.1608 $mmol \cdot gDW^{-1} \cdot h^{-1}$ was
1214 established for the consideration of growth.

1215

1216 **Table legends**

1217

1218 **Table 1. *Xylella fastidiosa* strains used for the pangenome reconstruction and genome-**
1219 **scale metabolic modeling.** The complete genomes of eighteen strains of *X. fastidiosa*
1220 belonging to five subspecies of the phytopathogen were used for the reconstruction of the
1221 pangenome. For each case, the strain identifier, the subspecies to which it belongs, the host,
1222 the site of isolation, the disease it causes and the NCBI accession number for the genome are
1223 indicated.

Fig. 1

A

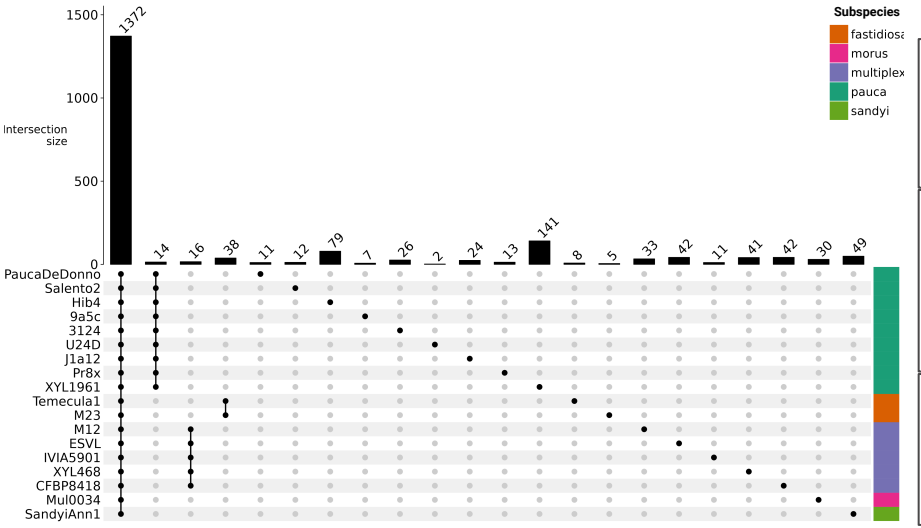

B

	iXfcore features	Count
Metabolites	Cytosol metabolites	1012
	Extracellular metabolites	63
	Unique metabolites	1013
	Total	1075
Reactions	Boundary reactions	69
	Transport reactions	76
	Biomass reactions	1
	Biochemical reactions	964 (888)
	Total	1034
Genes	Core genes	407
	Accessory genes	43
	Others	1
	Total	451

C

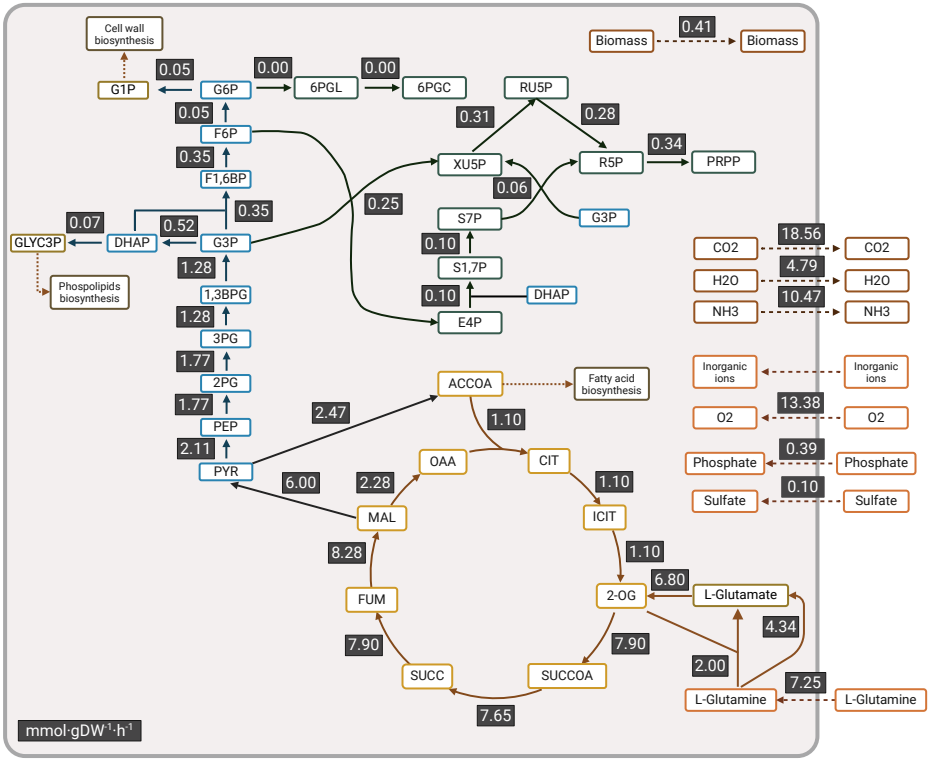

Fig. 2

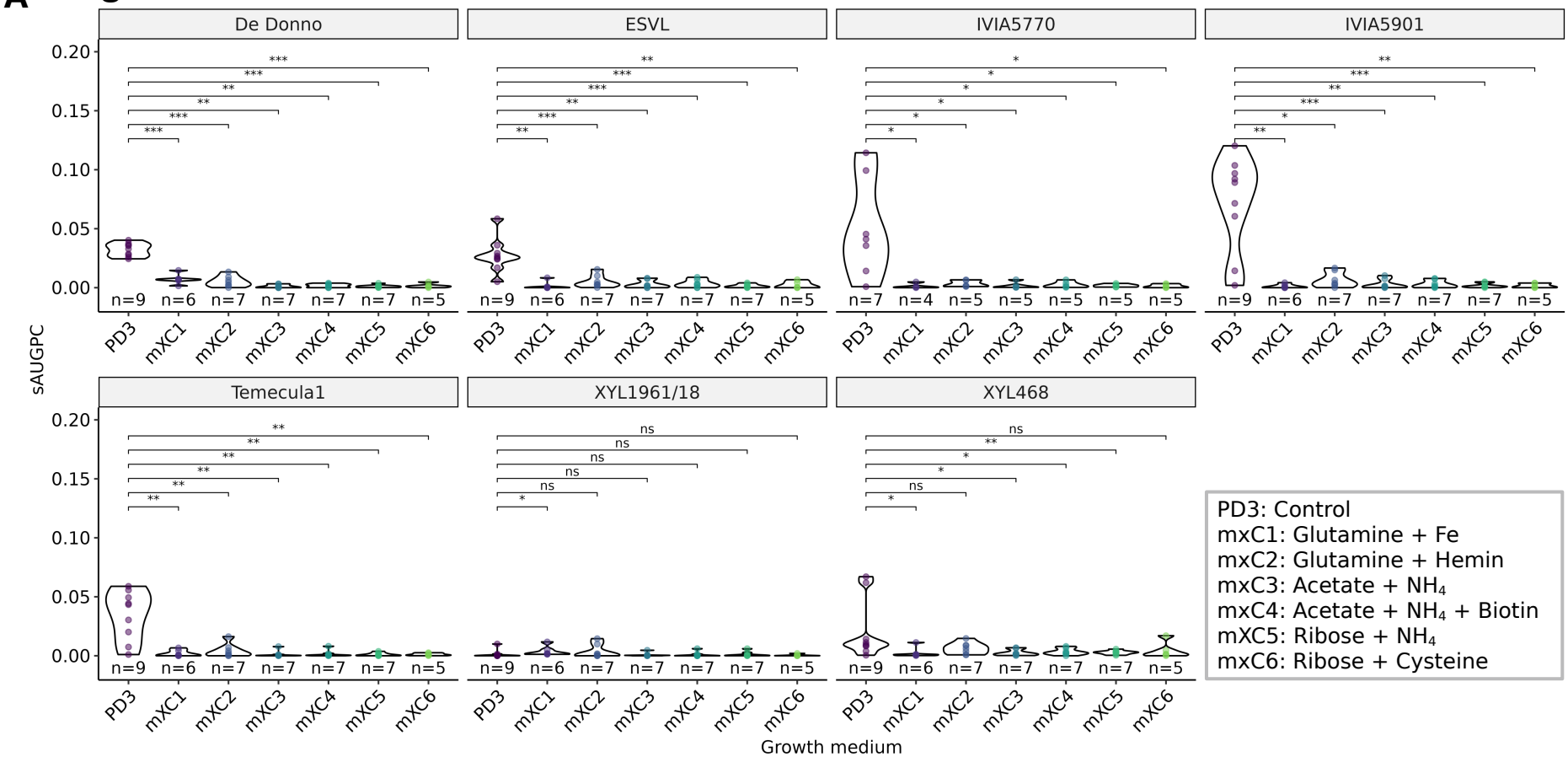
A
De Donno
ESVL
IVIA5770
IVIA5901
Temecula1
XYL1961/18
XYL468
sAUGPC
0.20
0.15
0.10
0.05
0.00
n=9 n=6 n=7 n=7 n=7 n=7 n=5
n=7 n=4 n=5 n=5 n=5 n=5 n=5
PD3 mXC1 mXC2 mXC3 mXC4 mXC5 mXC6
Growth medium
PD3: Control
mxC1: Glutamine + Fe
mxC2: Glutamine + Hemin
mxC3: Acetate + NH4
mxC4: Acetate + NH4 + Biotin
mXC5: Ribose + NH4
mxC6: Ribose + Cysteine

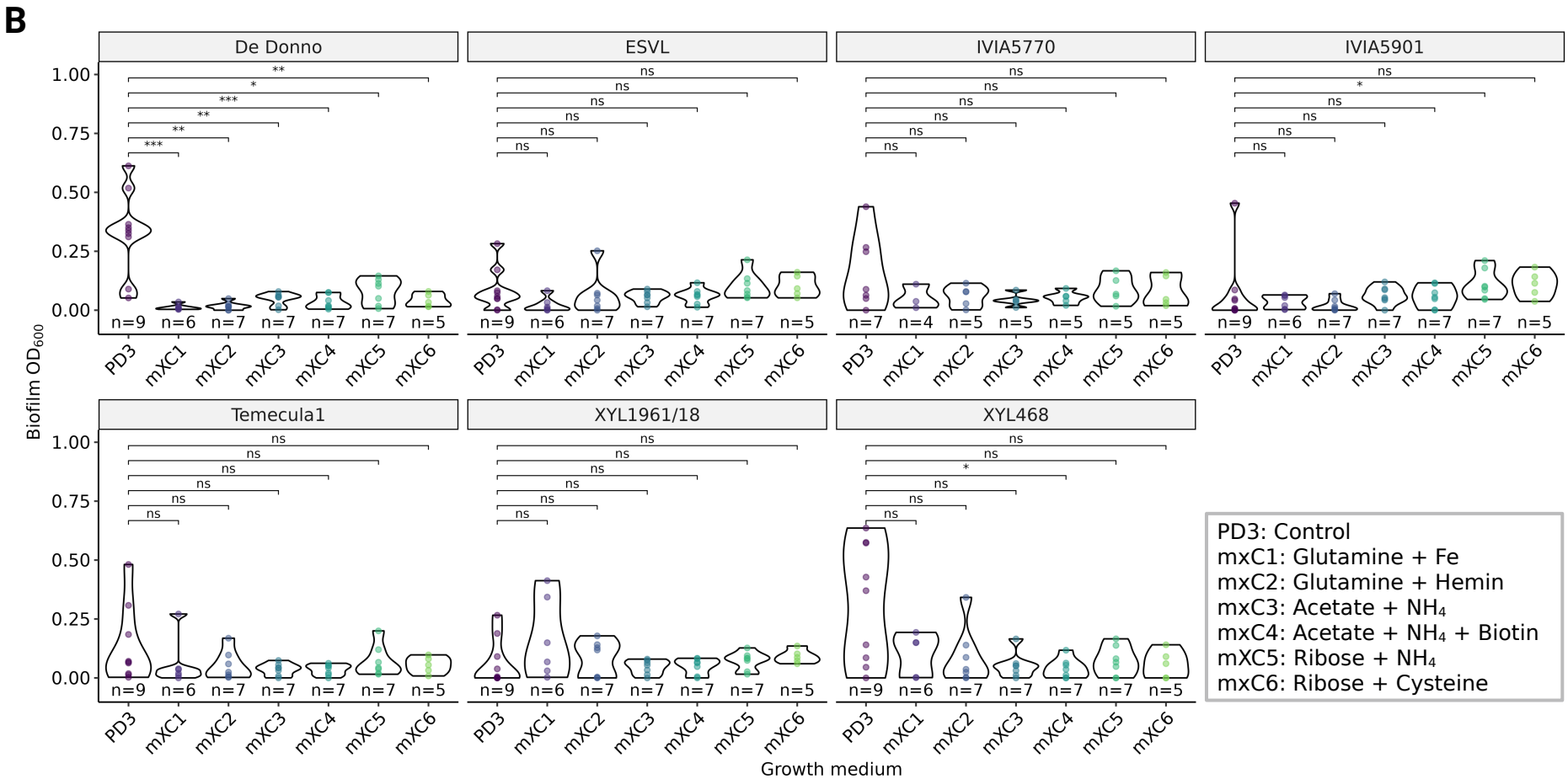
B
De Donno
ESVL
IVIA5770
IVIA5901
Temecula1
XYL1961/18
XYL468
Biofilm OD600
1.00
0.75
0.50
0.25
0.00
n=9 n=6 n=7 n=7 n=7 n=7 n=5
n=7 n=4 n=5 n=5 n=5 n=5 n=5
PD3 mXC1 mXC2 mXC3 mXC4 mXC5 mXC6
Growth medium
PD3: Control
mxC1: Glutamine + Fe
mxC2: Glutamine + Hemin
mxC3: Acetate + NH4
mxC4: Acetate + NH4 + Biotin
mXC5: Ribose + NH4
mxC6: Ribose + Cysteine

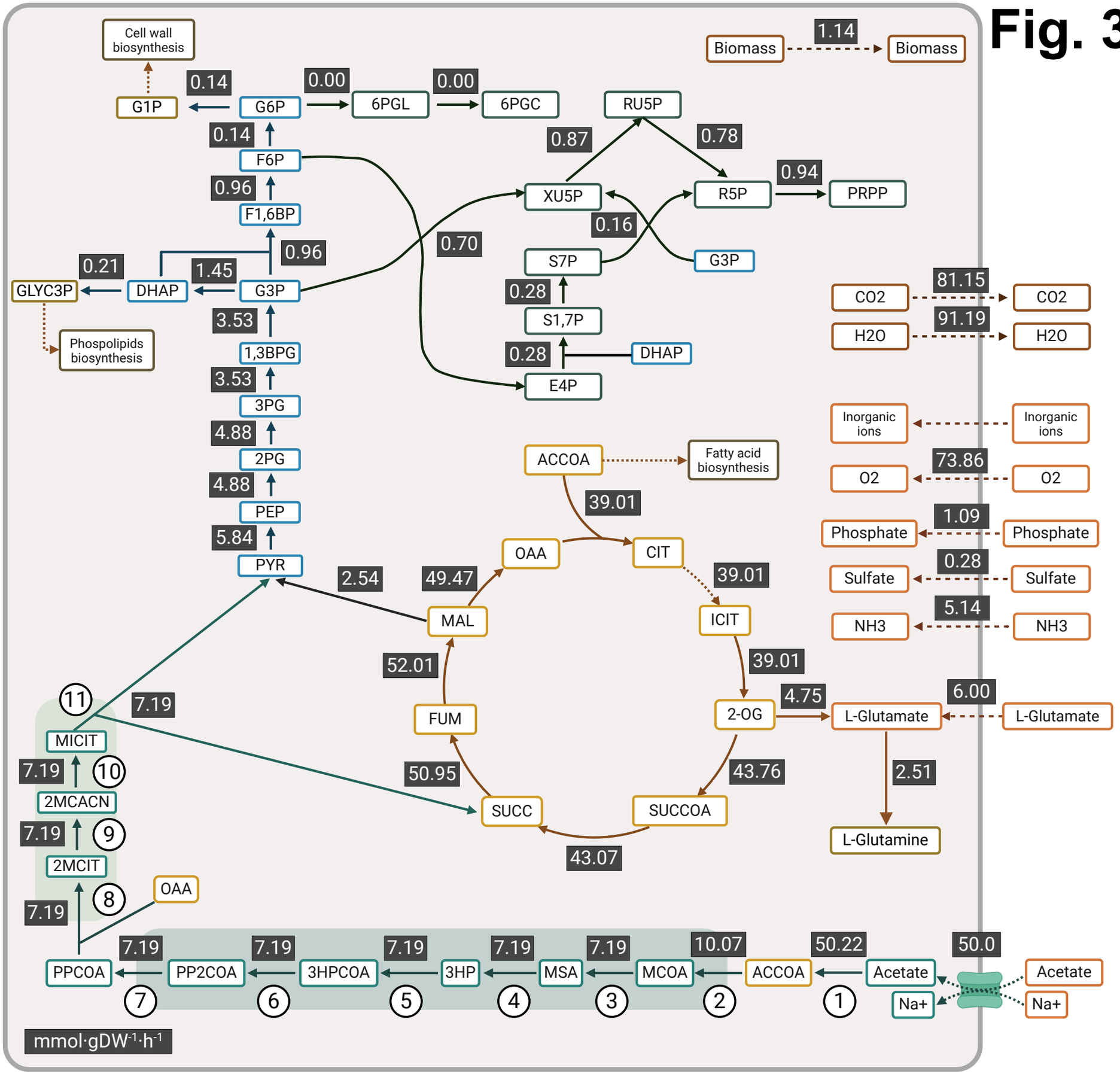
Fig. 3
Cell wall biosynthesis
G1P
0.14
G6P
0.00
6PGL
0.00
6PGC
Biomass
1.14
Biomass
RU5P
0.87
0.78
0.14
F6P
0.96
F1,6BP
XU5P
R5P
0.94
PRPP
0.16
0.70
0.96
S7P
G3P
0.21
1.45
GLYC3P
DHAP
G3P
0.28
S1,7P
3.53
Phospolipids biosynthesis
1,3BPG
0.28
DHAP
E4P
3.53
3PG
4.88
2PG
4.88
PEP
5.84
PYR
CO2
81.15
CO2
H2O
91.19
H2O
Inorganic ions
Inorganic ions
O2
73.86
O2
Phosphate
1.09
Phosphate
Sulfate
0.28
Sulfate
NH3
5.14
NH3
ACCOA
Fatty acid biosynthesis
39.01
OAA
CIT
39.01
2.54
49.47
MAL
ICIT
52.01
39.01
11
7.19
FUM
2-OG
4.75
6.00
L-Glutamate
L-Glutamate
MICIT
7.19
10
50.95
43.76
2.51
2MCACN
SUCC
SUCCOA
7.19
9
L-Glutamine
2MCIT
43.07
8
OAA
7.19
7.19
7.19
7.19
7.19
7.19
10.07
50.22
50.0
PPCOA
PP2COA
3HPCOA
3HP
MSA
MCOA
ACCOA
Acetate
Acetate
7
6
5
4
3
2
1
Na+
Na+
mmol·gDW-1·h-1
Gluconeogenesis
Krebs cycle
PPP pathway
Uptake
Secretion
3HP pathway
Methylcitrate pathway

Fig. 4

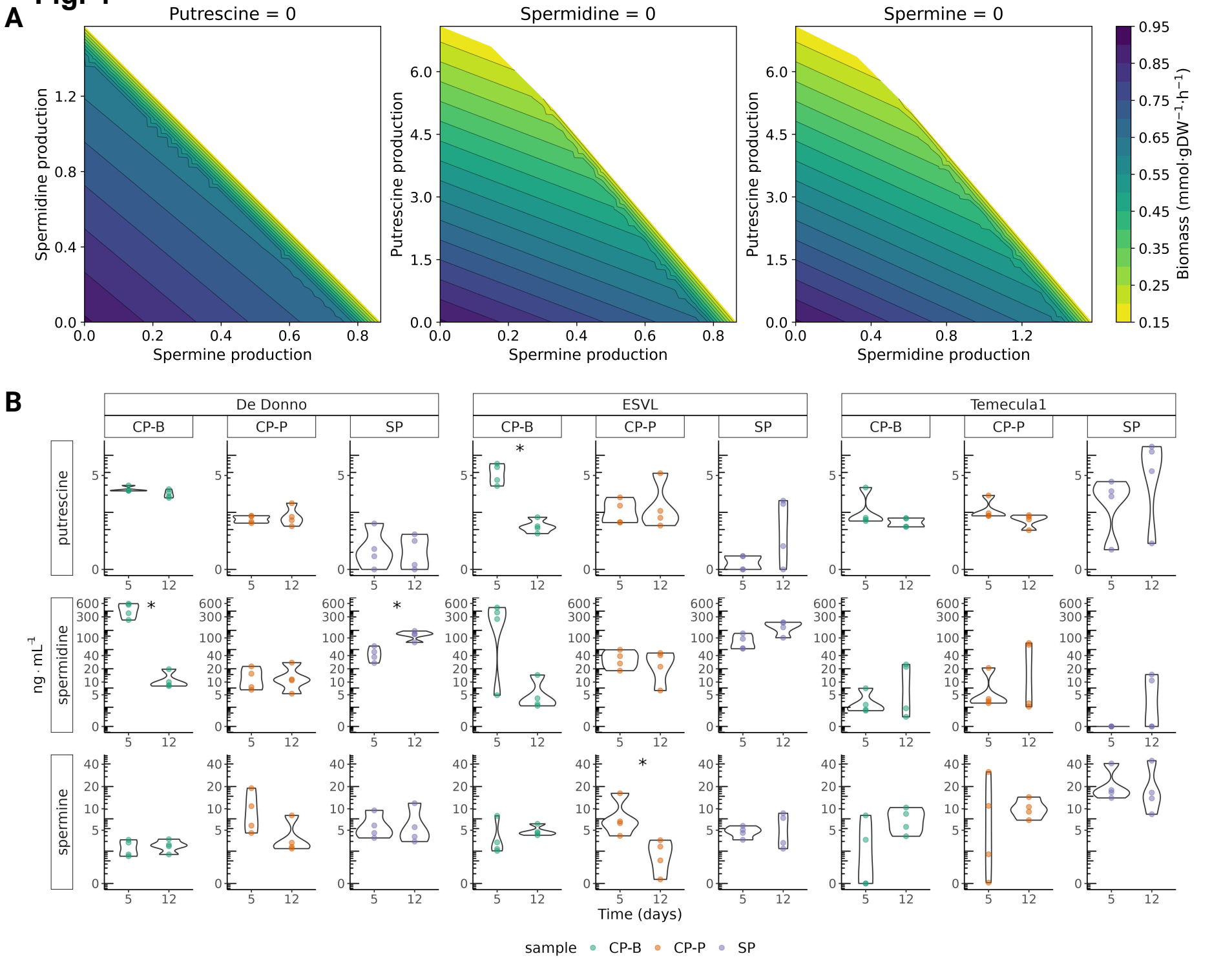
A
Putrescine = 0
Spermidine = 0
Spermine = 0
Spermidine production
Putrescine production
Spermine production
Spermidine production
Biomass (mmol·gDW⁻¹·h⁻¹)
B
De Donno
ESVL
Temecula1
CP-B
CP-P
SP
putrescine
spermidine
spermine
ng · mL⁻¹
Time (days)
sample
CP-B
CP-P
SP

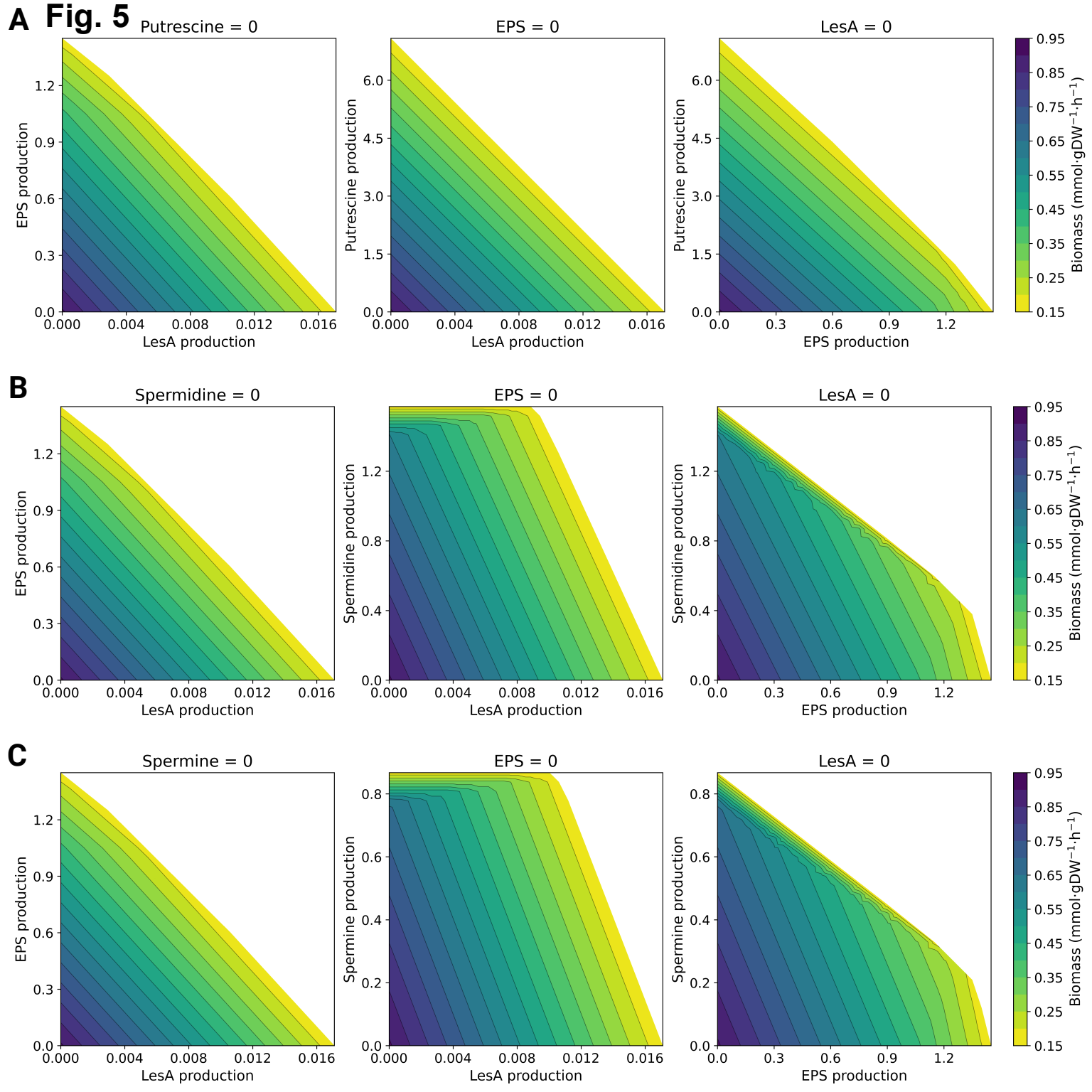
A
Fig. 5
Putrescine = 0
EPS = 0
LesA = 0
EPS production
Putrescine production
LesA production
EPS production
Biomass (mmol·gDW^{-1}·h^{-1})
B
Spermidine = 0
EPS = 0
LesA = 0
EPS production
Spermidine production
LesA production
EPS production
Biomass (mmol·gDW^{-1}·h^{-1})
C
Spermine = 0
EPS = 0
LesA = 0
EPS production
Spermine production
LesA production
EPS production
Biomass (mmol·gDW^{-1}·h^{-1})

1224 **Table 1.**

Identifier	Subspecies	Host	Location	Disease[a]	ID RefSeq
Temecula1	*fastidiosa*	*Vitis vinifera*	California, USA	PD	NC_004556.1
M23	*fastidiosa*	*Prunus dulcis*	California, USA	PD, ALS	NC_010577.1
MUL0034	*morus*	*Morus alba*	California, USA	MLS	NZ_CP006740.1
M12	*multiplex*	*Prunus dulcis*	California, USA	ALS	NC_010513.1
ESVL	*multiplex*	*Prunus dulcis*	Alacant, Spain	ALS	NZ_CP099516.1
IVIA5901	*multiplex*	*Prunus dulcis*	Alacant, Spain	ALS	NZ_CP047134.1
XYL468	*multiplex*	*Olea europaea var. sylvestris*	Mallorca, Spain	OQDS	NZ_CP136966.1
CFBP8418	*multiplex*	*Spartium junceum*	Corse, France	LS	NZ_CP136979.1
9a5c	*pauca*	*Citrus sinensis*	São Paulo, Brazil	CVC	NC_002488.3
U24d	*pauca*	*Citrus sinensis*	São Paulo, Brazil	CVC	NZ_CP009790.1
J1a12	*pauca*	*Citrus sinensis*	São Paulo, Brazil	Non-pathogenic	NZ_CP009823.1
Pr8x	*pauca*	*Prunus domestica*	São Paulo, Brazil	LS	NZ_CP009826.1
3124	*pauca*	*Coffee arabica*	São Paulo, Brazil	CLS	NZ_CP009829.1
Hib4	*pauca*	*Hibiscus fragilis*	Distrito Federal, Brazil	LS	NZ_CP009885.1
Salento-2	*pauca*	*Olea europaea*	Puglia, Italy	OQDS	NZ_CP016610.1
De Donno	*pauca*	*Olea europaea*	Puglia, Italy	OQDS	NZ_CP020870.1
XYL1961/18	*pauca*	*Olea europaea var. europaea*	Eivissa, Spain	OQDS	CP171775.1
Ann-1	*sandyi*	*Nerium oleander*	California, USA	OLS	NZ_CP006696.1

1225 [a] PD: Pierce's Disease; ALS: Almond Leaf Scorch; MLS: Mulberry Leaf Scorch; CVC: Citrus
1226 Variegated Chlorosis; CLS: Coffee Leaf Scorch; OQDS: Olive Quick Decline Syndrome; OLS:
1227 Oleander Leaf Scorch; LS: Leaf Scorch.